Defence Research and Development Canada
Recherche et développement pour la défense Canada

DEFENCE R&D DÉFENSE

A Target Simulation for Studies of Radar Detection in Clutter

Alan D. Thomson

Defence R&D Canada - Ottawa
TECHNICAL REPORT
DRDC Ottawa TR 2002-145
October 2002

Canada

A Target Simulation for Studies of Radar Detection in Clutter

Alan D. Thomson
Surface Radar Section

Defence R&D Canada – Ottawa

TECHNICAL REPORT

DRDC Ottawa TR 2002-145

October 2002

Abstract

A high fidelity simulation of the coherent signal samples produced by a low-PRF shipborne pulsed Doppler radar when observing a sea-skimming anti-ship missile moving through precipitation above the sea has been created. The modelled radar system uses a phased array antenna and has the ability to vary the parameters of the transmitted waveform from burst to burst. The output of the simulation is designed for combination with the output of clutter and signal processor simulations so that target detection in clutter can be examined. A complete description of the physical models used in the simulation and their mathematical implementation is presented. Example output data were used to derive propagation factor values, which were then compared with the output of the TERPEM commercial software package. Received power values were also derived from the example data and compared with the output of a multifunction radar simulator (ADAPT_MFR). Good agreement between the data sets was achieved, except for expected differences found at ranges near the radar horizon ("intermediate region"). Thus, this simulation is capable of producing realistic and useful signals for target detection studies. It is recommended that the simulation be upgraded by integrating the TERPEM software. This will allow propagation to be correctly considered near and beyond the radar horizon, thus extending the applicability of the simulation.

Résumé

Une simulation haute fidélité d'échantillonnage de signaux cohérent produit par un radar Doppler naval a basses fréquences de répétition de pulses observant un missile anti-navire qui se déplace au-dessus de la mer à travers des précipitations a été créée. Le modèle de système radar utilise une antenne à réseaux de phase et peut changer les paramètres de la forme d'onde transmise de groupe de pulses en groupe de pulses. Les sorties de la simulation sont choisies pour se combiner avec les sorties de fouillis et les simulations de traitement de signaux de façon que la détection de cible dans un fouillis puisse être étudier. Une description complète des modèles physiques utiliser dans la simulation et leur représentation mathématique est présentée. Des données de sorties ont été utilisées pour dériver des valeurs de facteur de propagation, lesquelles ont été comparées avec les sorties du programme commercial TERPEM. Les valeurs de pouvoir reçus ont été aussi dériver de ces données et compare avec les sorties du simulateur de radar multifonction (ADAPT_MFR). Un bon accord entre ces groupe de données a été produit, exceptée pour une différence prévu au distance proche de l'horizon radar (région intermédiaire). Ainsi, cette simulation est capable de produire des signaux réaliste et utile pour des études de détection de cibles. Il est recommandé que la simulation soit améliorer en intégrant le logiciel TERPEM. Cela permettra a la propagation d'être considérer correctement proche et au delà de l'horizon radar, ainsi élargissant les applicabilités de cette simulation.

This page intentionally left blank.

Executive Summary

Recent emphasis on naval operations in the littoral zone and the potent threat of sea-skimming anti-ship missiles has increased the importance of understanding the capability of radar to detect small targets in highly cluttered environments. Simulation is a useful approach for developing an initial assessment of radar detection performance, since acquiring real shipborne radar measurements of sea-skimming missiles in littoral clutter is a major undertaking. In addition, it would be very difficult to acquire, experimentally, a data set encompassing the full range of clutter conditions that shipborne radar must operate in.

This report describes a high fidelity simulation of the received signals produced by shipborne radar when observing a sea-skimming anti-ship missile moving through precipitation above the sea. The simulation was designed as a component of a larger simulation aimed at determining the detection performance of radar operating in clutter conditions. The physical models used in the simulation and their mathematical implementation is described.

This report also presents an evaluation of the target simulation by comparing quantities derived from example output data with similar data generated by a commercial software package, and by a lower fidelity multifunction radar simulation. Good agreement was achieved in each comparison, except where the calculations were extended to the radar horizon. It is recommended that this simulation be integrated with the commercial software package TERPEM, so that its applicability can be extended to any range near or beyond the radar horizon and to any atmospheric structure. Nevertheless, the favourable comparisons in the interference region demonstrate that this simulation is accurate, where applicable, and that it can be used with confidence for its stated purpose of assessing radar detection performance in clutter.

Thomson, A. D., 2002. A Target Simulation for Studies of Radar Detection in Clutter. DRDC Ottawa TR 2002-145. Defence R&D Canada – Ottawa.

Sommaire

L'emphase récente sur les opérations navales en région littorale et la menace existante des navires anti-navire a augmenté l'importance de comprendre la capacité des radars pour détecter des cibles petites dans des fouillis important. La simulation est une approche utile pour développer une évaluation initiale de la performance de détection radar, puisque l'acquisition de donnée réelle de mesures de radar navales de missile anti-navire volant dans un fouillis littoral est un effort considérable. De plus. Il serait très difficile d'obtenir expérimentalement un ensemble de données incluant la grande variété de conditions de fouillis qu'un radar naval peut rencontrer.

Ce rapport décrit une simulation haute fidélité d'échantillonnage de signaux reçus par un radar naval qui observe un missile anti-navire se déplaçant a travers des précipitations au dessus de la mer. La simulation a été conçue comme une composante d'un plus gros simulateur pouvant déterminer la performance de détection de radar opérant dans des conditions de fouillis. Une description complète des modèles physiques utiliser dans la simulation et leur représentation mathématique est décrite.

Ce rapport présente aussi une évaluation de la simulation en comparant des quantités dérivées d'exemple spécifique avec des quantités similaires générer par un logiciel commercial, et un simulateur de radar multifonction basse fidélité. Un bon accord a été produit pour chaque comparaison, excepte pour les calculs au-delà de l'horizon radar. Il est recommandé que la simulation soit améliorer en intégrant le logiciel TERPEM, ce qui permettra d'étendre ses applicabilités à des distances proche ou au delà de l'horizon radar et aussi pour n'importe quelle structure atmosphérique. Cependant, les comparaisons favorables dans la région d'interférence intermédiaire démontrent que cette simulation est précise, quand applicable, et qu'elle peut être utiliser avec confiance pour l'évaluation de performance de détection de cible en fouillis.

Thomson, A. D., 2002. A Target Simulation for Studies of Radar Detection in Clutter. DRDC Ottawa TR 2002-145. R & D pour la défense Canada – Ottawa.

Table of Contents

List of Figures

List of Tables

This page intentionally left blank.

1 Introduction

Recent emphasis on naval operations in the littoral zone and the potent threat of sea-skimming anti-ship missiles has increased the importance of understanding the capability of radar to detect small targets in highly cluttered environments. Simulation is a useful approach for developing an initial assessment of radar detection performance, since acquiring real shipborne radar measurements of sea-skimming missiles in littoral clutter is a major undertaking. In addition, it would be very difficult to acquire, experimentally, a data set encompassing the full range of clutter conditions that shipborne radar must operate in.

This report describes a high fidelity simulation of the coherent signal samples produced by shipborne low-PRF radar when observing a sea-skimming anti-ship missile moving through precipitation above the sea. The simulation was designed as a component of a larger simulation aimed at determining the detection performance of radar operating in clutter conditions. The physical models used in the simulation and their mathematical implementation is described. These models are the same as or compatible with the models used in the other components of the larger detection simulation. In some cases these models represent upgraded versions of models previously described for the weather clutter simulation component [1]. In such cases the upgraded models have also been applied to the weather clutter simulation. Hence, this report serves as a description of upgrades to the weather clutter simulation. This report also presents an evaluation of the target simulation by comparing propagation factor values derived from example output with data generated by the commercial software package TERPEM. In addition, the received power data generated by the target simulation are compared with similar data generated by a multifunction radar simulation (ADAPT_MFR, Jones et al. [2]).

2 General Approach

The geometry of the general scenario that is modelled by the target simulation is depicted in Figure 1. A sea-skimming missile flies at constant altitude above the sea directly toward the radar system attempting to detect it. The azimuth of the missile approach also remains constant with respect to the radar. This corresponds to a worst-case detection scenario in terms of the radar cross-section of the missile. The simulation could be expanded to include manoeuvring targets if the radar cross-section of the target was known as a function of aspect angle. Figure 1 also shows that the missile, which moves at a constant velocity, has a different position each time it is illuminated by a radar pulse.

The modelled atmosphere is composed of gases, clouds, and precipitation that will attenuate the signals transmitted by the horizon scanning radar. Clutter returns and radar system noise are generated by the other simulations that makeup the overall detection simulation (e.g., see Thomson [3]). Propagation is currently considered in a simplistic manner. Refraction of the radar signal is considered using an effective earth radius. Interference caused by reflection of the signal from the sea surface is calculated geometrically. Diffraction by the sea surface is neglected, which places important limitations on the applicability of this simulation. Specifically, this approach can only be used in the "interference region" (see Blake [4], p. 269-279). When the modelled target is within the "intermediate region", near the radar horizon, the limited propagation calculations will be incorrect. This is not considered to be a major problem when investigating radar detection of targets within strong clutter since in most cases the clutter will prevent detection of the target in the intermediate region anyway. However, care should be used when analyzing detection results to ensure that target detections within the intermediate region are properly considered.

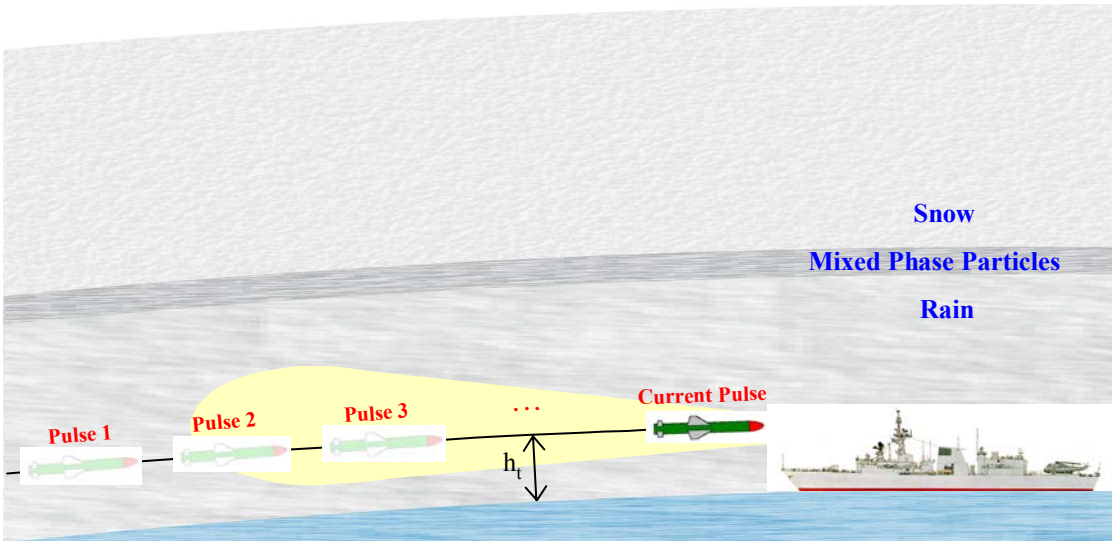

Figure 1. *The general scenario modelled by the target simulation. Blue shading depicts the spherical sea surface. Grey shading depicts the three phases of precipitation in the atmosphere. The thin black line depicts the missile trajectory at a constant altitude along a constant azimuth with respect to the radar.*

The main outputs of the simulation are the discrete in-phase, I_n, and quadrature, Q_n, components representing the voltage signal received by the radar when observing the target. I_n and Q_n values are calculated for the range bins of each scan in which the missile is illuminated by the radar. These range bins will only be found in the radar beam that covers the constant azimuth of the missile approach.

Figure 2 presents an overview of the mathematical approach used to calculate the target signals. Although the simulation produces signals for many range bins in many different scans, the figure only depicts the process for one range bin. The process begins with a missile model and a statistical model.

The missile model calculates the mean in-phase, $\bar{I}_n$, and quadrature, $\bar{Q}_n$, components of the target signal. These calculations consider the transmit and receive characteristics of the radar, attenuation of the signal by the precipitation field, the target characteristics, the sea surface conditions, and multipath interference caused by a reflective sea surface. Details of these calculations are given in Section 5.

The modelled missile can be considered to have several different scattering features. Consequently, as the orientation of the missile changes with respect to the radar, the interference of the waves backscattered from the different scattering features will vary. The statistical model creates random numbers that represent the time varying fluctuations in the radar signal that result when the interfering waves are summed at the antenna port. The rate of fluctuation and the statistical properties of the random numbers output by the statistical model correspond to the four Swerling models (see Skolnik [5]). The particular Swerling

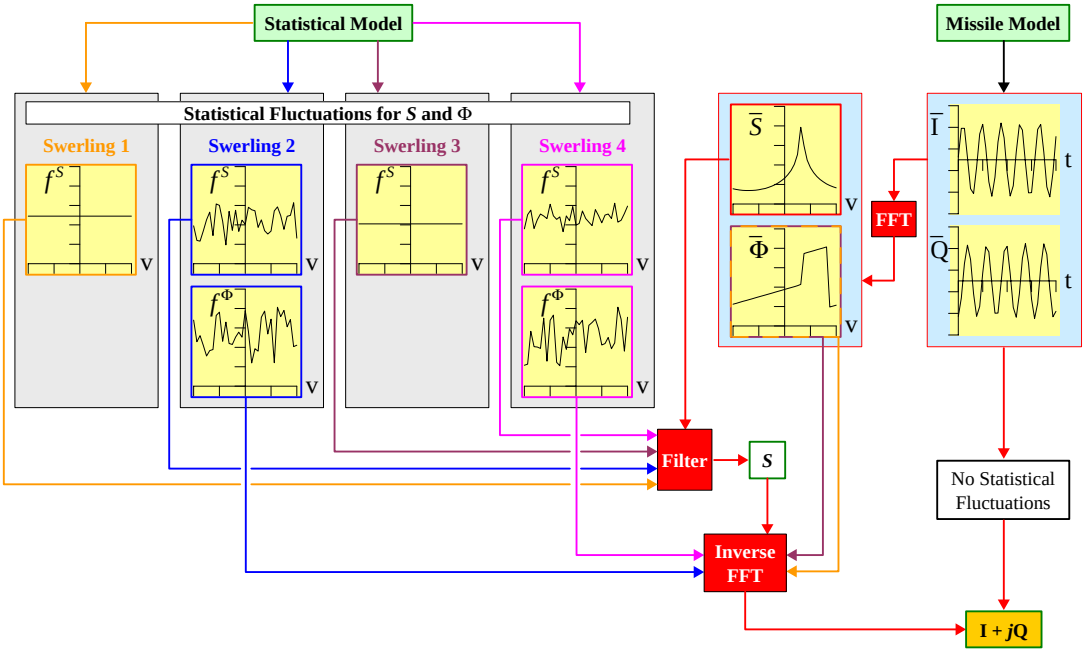

Figure 2. *Overview of the computational approach used to generate the target signals. Here the dimension of the abscissa in the power and phase spectra plots is Doppler velocity,* v*, as opposed to Doppler shift frequency.*

model used is an input parameter specified by the user. In addition, the user may also specify a non-fluctuating target model in which the overall I_n and Q_n output of the target model is taken directly from the missile model, i.e., $I_n = \bar{I}_n$ and $Q_n = \bar{Q}_n$. Specifically, the statistical model creates vectors of random numbers, each N_c elements long, for each range bin where the target signal is non-zero. Here N_c denotes the number of coherent pulses per burst transmitted by the radar. The two sets of random numbers, $\vec{f}^{\,S} = \left(f_0^S, f_1^S, \ldots, f_i^S, \ldots, f_{N_c-1}^S\right)$ and $\vec{f}^{\,\Phi} = \left(f_0^\Phi, f_1^\Phi, \ldots, f_i^\Phi, \ldots, f_{N_c-1}^\Phi\right)$, represent the fluctuations in the power and phase spectra, respectively, of the target signal. Details of the statistical model are given in Section 6.

The coefficients of the mean power and phase spectra, $\bar{S}_i$ and $\bar{\Phi}_i$, of the missile signal corresponding to a particular range bin are calculated from $\bar{I}_n$ and $\bar{Q}_n$ using a discrete Fourier transform (**DFT**), i.e.,

$$\begin{aligned} \bar{S}_i &= \left(\mathbf{Re}\left\{\bar{X}_i\right\}\right)^2 + \left(\mathbf{Im}\left\{\bar{X}_i\right\}\right)^2 \\ \bar{\Phi}_i &= \tan^{-1}\left(\frac{\mathbf{Im}\left\{\bar{X}_i\right\}}{\mathbf{Re}\left\{\bar{X}_i\right\}}\right) \end{aligned} \tag{1}$$

where

$$\bar{\bar{X}} = \mathbf{DFT}\left\{\bar{\bar{I}} + j\bar{\bar{Q}}\right\} \qquad j = \sqrt{-1} \tag{2}$$

and **Re** and **Im** take the real and imaginary part of their respective arguments. The signals $\bar{\bar{I}}$ and $\bar{\bar{Q}}$ also contain N_c elements each, i.e.,

$$\begin{aligned} \bar{\bar{I}} &= \left(\bar{I}_0, \bar{I}_1, \ldots, \bar{I}_n, \ldots, \bar{I}_{N_c-1}\right) \\ \bar{\bar{Q}} &= \left(\bar{Q}_0, \bar{Q}_1, \ldots, \bar{Q}_n, \ldots, \bar{Q}_{N_c-1}\right) \end{aligned} \tag{3}$$

The statistical fluctuations are incorporated into the simulated target signal by filtering $\vec{f}^{\,S}$ with $\bar{\bar{S}}$, i.e., the power spectrum coefficients are given by

$$S_i = \bar{S}_i f_i^S \tag{4}$$

The phase spectrum of the final target signal is given by the mean phase spectrum, $\bar{\bar{\Phi}}$, for Swerling cases 1 and 3, and is given by the phase fluctuations, $\vec{f}^{\,\Phi}$, for Swerling cases 2 and 4. The final I_n and Q_n signal samples are calculated by inverse **DFT**, i.e.,

$$\vec{\mathrm{I}} = \mathbf{Re}\left\{\mathbf{DFT}^{-1}\left\{\vec{\mathrm{X}}\right\}\right\}$$
$$\vec{\mathrm{Q}} = \mathbf{Im}\left\{\mathbf{DFT}^{-1}\left\{\vec{\mathrm{X}}\right\}\right\} \tag{5}$$

where

$$\mathrm{X}_i = \sqrt{S_i}\,\exp\left(j\,\overline{\Phi}_i\right) \qquad \text{for Swerling 1 and 3 cases}$$
$$\mathrm{X}_i = \sqrt{S_i}\,\exp\left(j\,f_i^{\Phi}\right) \qquad \text{for Swerling 2 and 4 cases} \tag{6}$$

3 Environment Model

The modelled environment is the same as that used in the weather clutter simulation that also forms a part of the larger detection simulation referred to earlier (e.g., see Thomson [3]). A complete description of the modelled environment and its effects on the radar signal are given in Thomson [1]. Only a brief summary will be given here.

The modelled environment consists of a stratiform precipitation field above a rough spherical sea surface. The precipitation field consists of horizontally homogeneous layers of rain, mixed phase particles, and snow. A uniform cloud field also exists from a specified lower level to the top of the snow layer. The input parameters required to specify this environment are listed in Table 1.

The quantity $Z(h)$ shown in Table 1 denotes the height profile of reflectivity factor where h is height above sea level. The reflectivity factor is related to the backscatter cross section of the precipitation (see Doviak and Zrnić [6]) and provides a measure of the precipitation intensity. For example, Z is often related to the rain rate, R, through a power law, i.e., $Z = aR^b$. The input Z profile is extrapolated horizontally to apply to any location within the viewing space of the radar. An example profile is shown in Figure 3. In this example, the snow region is characterized by decreasing Z above 4.0 km altitude. The region of larger Z between 3.4 and

Table 1. *Parameters describing the environment.*

SYMBOL	EXAMPLE VALUE	DESCRIPTION
c	3.0×10^8 m s^{-1}	speed of light
R_e	$\frac{4}{3} \times 6.37 \times 10^6$ m	effective earth radius
M_c	0.1 g m^{-3}	cloud liquid water content
$\lvert K_w \rvert^2$	0.92	complex refractive index function for water
a	200 mm^6 m^{-3} (mm h^{-1})$^{-b}$	Z-R power law coefficient*
b	1.6	Z-R power law exponent*
h_0	4000 m	height of 0 °C level
h_m	20000 m	maximum height of precipitation
h_b	25 m	cloud base height
t_b	600 m	thickness of the melting layer
$Z(h)$	see Figure 3	reflectivity factor profile
T_{sea}	28 °C	sea surface temperature
s	34 ppt	sea surface salinity in parts per thousand (ppt)
H_s	1	sea state

*$Z = a R^b$

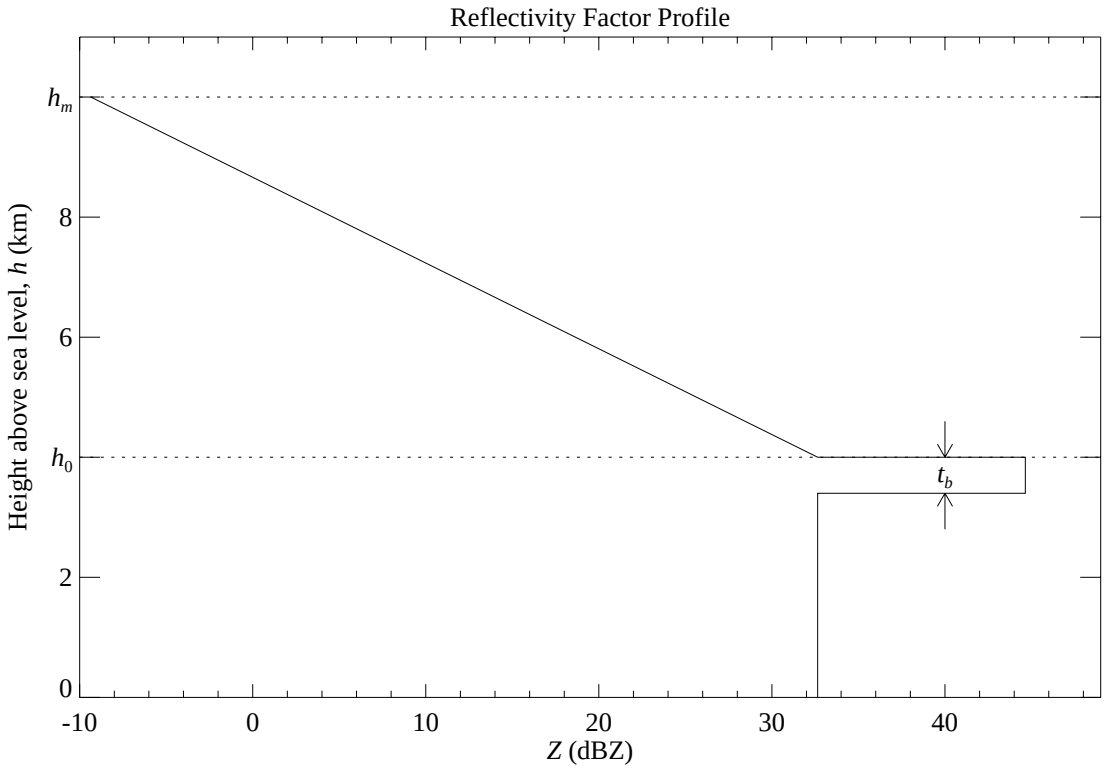

Figure 3. *Example height profile of reflectivity factor, Z, where* dBZ = 10.0 log(Z in mm^6 m^{-3})

4.0 km is where the snow melts into rain. The rain only region is below 3.4 km altitude.

The main effect of the precipitation field on the target signal is attenuation of the received power. The amount of attenuation is a function of the transmitted frequency and polarization, the cloud liquid water content, the precipitation rates, and the specific path travelled by the radar signal through the atmosphere. The end of the signal path is the location of the target as specified by the range vector $\vec{r}_t$. Thus, an attenuation value, $L_a(\vec{r}_t)$, is calculated for each missile position or equivalently for each transmitted radar pulse. The empirical models and mathematical approach used for these calculations are described in detail in Thomson [1].

4 Radar Model

The radar model of this simulation is very similar to that which was described for the weather clutter simulation in Thomson [1]. Most of the differences are a result of upgrades that were added to allow the radar model to be more generally applicable. Upgrades related to the range weighting function and the antenna gain pattern have also been implemented within the current version of the weather clutter simulation. Thus, the descriptions given in Sections 4.3 and 4.4 also apply to the current version of the weather clutter simulation.

The main remaining difference between the two radar models is the complexity of the transmitted waveform. The model presented here considers a multiple burst waveform in which the frequency, pulse repetition time, and the number of pulses per coherent burst change from burst to burst. The bursts are grouped into dwells so that an M-of-N detection scheme can be applied later. The waveform parameters describing the bursts can also vary from dwell to dwell. In addition, all of the signal samples for all dwells are calculated together for the entire target approach. In the case of the weather clutter simulation only a single burst is simulated. The more complex waveform used in this target simulation can still, however, be modelled by the weather clutter simulation, but this requires the weather clutter simulation, as it has been described in Thomson [1], to be executed multiple times; once for each burst. Thus, the outputs of the two simulations are compatible and can be combined as described in Thomson [3].

4.1 System parameters

The parameters used to describe a radar system are shown in Table 2. These example waveform parameters only specify a single burst. Section 4.2 discusses the full flexibility of the transmitted waveform. The peak gain on boresight, as well as the azimuth and elevation beamwidths, are calculated as a function of frequency as discussed in Section 4.4.

Pulse compression is modelled using a simplistic approach (see Barton [7], p 367) similar to that used in the weather clutter simulation (Thomson [1]). The compressed pulse is assumed to have the same properties as the uncompressed pulse, except for its length and transmitted power. The compressed pulse length is given by $\tau_c = \tau / P_c$, where P_c is the pulse compression ratio and τ is the uncompressed pulse length. The compressed pulse width is then used in all calculations, such as the range weighting function. This approach ignores the effects of range sidelobes. The increase in transmitted power associated with pulse compression is modelled by including a factor of P_c in the equation used to calculate received power (see Equation (36)). This approach assumes that the missile is a coherent target for a time period greater than τ.

In the case of the weather clutter simulation as described in Thomson [1], pulse compression was implicitly modelled by inputting appropriately scaled parameters into the simulation, i.e., τ / P_c, was entered for the pulse length, and $P_c^2 P_t$ was entered for the transmitted power. In this simulation, however, an input parameter for pulse compression is required and the

Table 2. *Parameters describing the radar.*

SYMBOL	EXAMPLE VALUE	DESCRIPTION
h_a	25 m	antenna height above sea level
ψ_c	15°	antenna cant back angle
ϕ_b	100°	azimuth of antenna boresight
P_t	17.12 kW	transmitted power
Θ	90° (vertical)	transmitted polarization
τ	50 μs	uncompressed pulse width
P_c	250	pulse compression ratio
τ_c	200 ns	compressed pulse width
G_{sys}	60 dB	receiver system gain
B_6	4 MHz	6 dB receiver bandwidth
G_b'	37.45 dB	antenna gain on boresight at f_g
f_g	10.0 GHz	frequency corresponding to boresight gain specification
G_f	1.0459076	fit parameter for antenna gain pattern
$\phi_{6b}(f_t)$	2.6471614	6 dB azimuth beamwidth on boresight
$\theta_{6b}(f_t)$	2.2864836	6 dB elevation beamwidth on boresight
$\Delta\phi_s$	90°	azimuth extent of scan area
θ_c	0°	elevation of beam axis when target is illuminated
ϕ_c	130°	azimuth of beam axis when target is illuminated
r_{min}	7.545 km	minimum range of horizon search
r_{max}	29.745 km	maximum range of horizon search
Δr	30 m	distance between the centres of adjacent range bins
T_s	240.7 μs	pulse repetition time
f_t	10.93 GHz	transmitted frequency
N_c	26	number of pulses per coherent burst

necessary calculations are performed within the simulation. Note that in Thomson [1] (see Section 6.1) P_t was scaled by P_c^2 whereas in this document P_t is scaled by P_c to model pulse compression. This scaling (P_c^2) could also be considered to give correct results if the extra factor of P_c is thought of as system gain, since in Thomson [1] the noise figure was also scaled by a factor of P_c. However, this extra scaling is unnecessary and is no longer used. Pulse compression in the upgraded weather clutter simulation would now be implemented by

using the compressed pulse length as the input pulse length and $P_c P_t$ as the input transmitted power. The noise figure would not be scaled.

4.2 Transmitted waveform

The transmitted waveform is defined by the parameters shown in Table 2. However, as stated earlier T_s, f_t, and N_c can be varied from burst to burst and from dwell to dwell. Three levels of complexity are possible. First the waveform parameters can remain constant so that only a single burst is defined and is transmitted repeatedly until the target reaches the minimum range, r_{min}. Second, a set of N_b values for each of T_s, f_t, and N_c can be defined. This results in a transmitted dwell consisting of N_b bursts. This dwell waveform is then transmitted repeatedly. Finally, a set of $N_b \times N_d$ values can be defined for each of T_s, f_t, and N_c. This results in N_d dwells being transmitted where each dwell contains N_b bursts and all bursts can be unique. If, in this case, the required transmission time for all defined dwells is shorter than the time required for the target to reach the minimum range, then the dwells will be repeated in order of their definition.

4.3 Range weighting function

An individual I or Q sample corresponding to a given range bin represents the integration of the received signal voltage over a finite period of time, which corresponds to a finite range increment. Therefore, the backscattered signals from all scatterers within this range increment will contribute to the signal sample. The range weighting function, W^2, describes the relative contribution to the signal sample of each scatterer's backscattered power based on the position of the scatterer with respect to the range, r_c, corresponding to the sample time.

The only scatterers considered in this simulation are the different scattering centres of the single target approaching the radar. These scatterers are modelled as a single point scatterer with the effect of the multiple scattering centres of the target being generated statistically (see Section 5). Thus, the entire target is assumed to be completely within the resolution volume corresponding to the signal sample. The weight, $W^2(r_t, r_c)$, for the point target at range, r_t, is applied to the received power calculated via the radar equation (see Equation (36)).

The specific form of the range weighting function used in this simulation is taken from Doviak and Zrnić [6], i.e.,

$$W^2(r, r_c) = \frac{1}{4}\left\{ \operatorname{erf}\left[\left(\frac{\pi B_6}{c\sqrt{\ln 2}} \right) \left(r_c - r + \frac{c\tau_c}{4} \right) \right] - \operatorname{erf}\left[\left(\frac{\pi B_6}{c\sqrt{\ln 2}} \right) \left(r_c - r - \frac{c\tau_c}{4} \right) \right] \right\}^2 \tag{7}$$

where c is the speed of light, and "erf" is the error function given by

$$\operatorname{erf}(x) = \frac{2}{\sqrt{\pi}} \int_0^x \exp\left(-y^2\right) \mathrm{d}y \tag{8}$$

Equation (7) corresponds to the case of a rectangular transmitted pulse and a practically matched receiver having a Gaussian frequency response.

This form of the range weighting function is also used in the current version of the weather clutter simulation. The single difference between Equation (7) and its counterpart that is described in Thomson [1] is the decoupling of B_6 and τ_c.

Figure 4 shows a plot of Equation (7) for the case defined by the parameters in Table 2. The 6 dB range width of the resolution volume, R_6, is determined by solving the transcendental equation

$$W^2\left(r_c, r = r_c + \frac{R_6}{2}\right) = \frac{1}{4} W^2\left(r_c, r = r_c\right) \tag{9}$$

For B_6 = 4.0 MHz, τ_c = 200 ns, and any value of r_c, R_6 = 39.806892 m, which, as shown in Figure 4, is greater than $c\tau_c/2 = 30$ m. The target simulation only considers the portion of the resolution volume within the 6 dB range points, $r_c \pm R_6/2$, as is the case for the weather clutter simulation. For the case defined in Table 2, R_6 is also greater than the distance between the centres of adjacent range bins, Δr. Thus, in this case, there is some overlap between adjacent range bins.

4.4 Antenna gain pattern

The radar antenna is modelled as an elliptical phased array. The corresponding radar beam has frequency dependent beamwidths that increase and a frequency dependent peak gain that

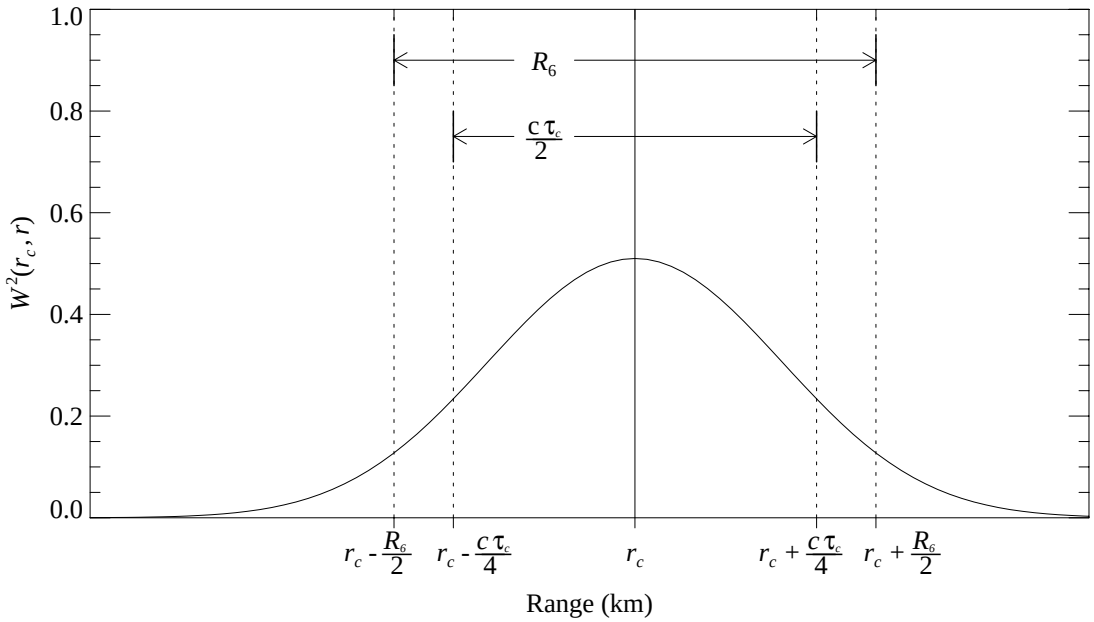

Figure 4. *The range weighting function.*

decreases as the beam is scanned away from the boresight.

The geometry of the phased array antenna is shown in Figure 5. Here the antenna face is shown as an elliptical aperture canted back by an angle ψ_c with respect to the z-axis. The unit vector $\hat{r}_b$ defines the direction of the antenna boresight in a coordinate system that has its origin at the centre of the antenna. The angle ϕ_b specifies the azimuth of the antenna boresight.

The target simulation only considers the portion of the resolution volume that receives a weight, specified by the radar transmit/receive characteristics, that is within 6 dB of the weight applied to the centre of the resolution volume at spherical polar coordinates (r_c, θ_c, ϕ_c). Therefore, the antenna gain pattern must be specified over the angular range defined by the 3 dB elevation and azimuth beamwidths, θ_3 and ϕ_3. A two dimensional Gaussian function is used to describe the far-field 1-way antenna gain pattern in this region, i.e.,

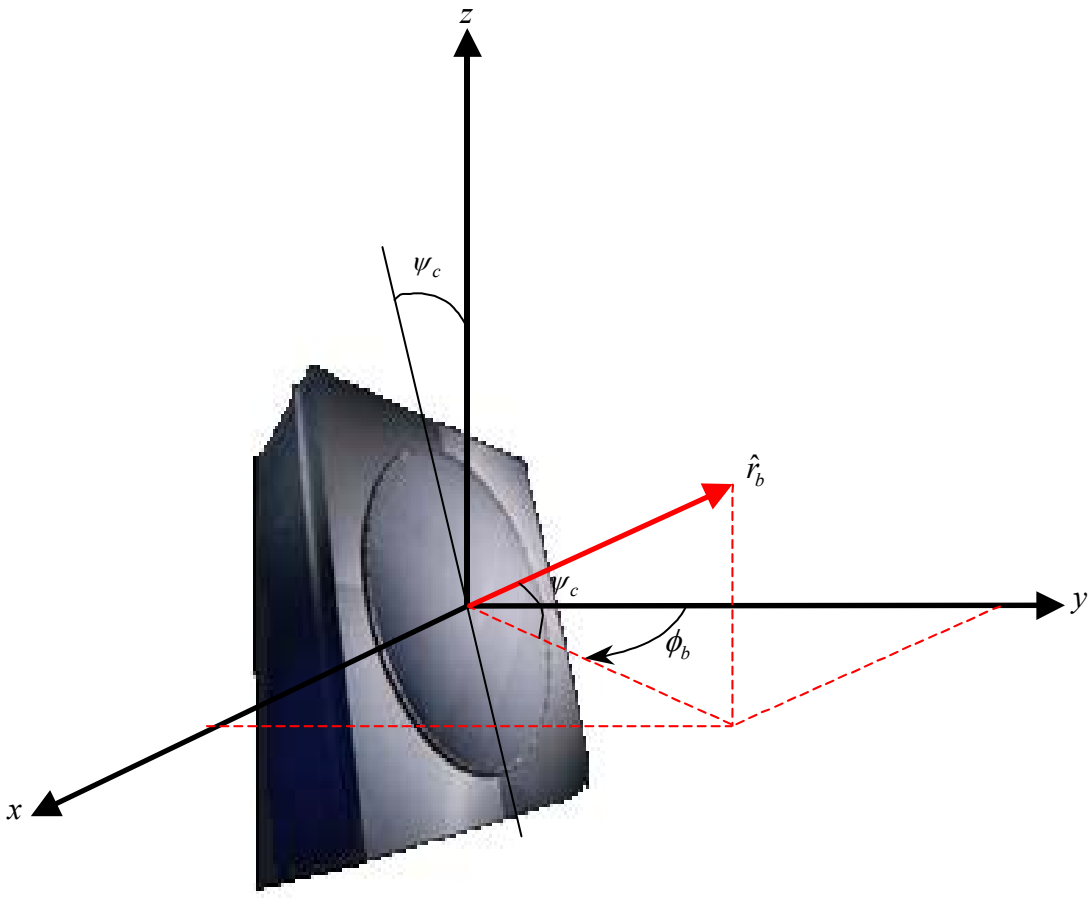

Figure 5. *Antenna geometry.*

$$G(\theta,\phi,\theta_c,\phi_c) = G_f\ G_s \exp\left\{-8\ln 2\left[\frac{|\theta-\theta_c|^2}{\theta_6^2}+\frac{|\phi-\phi_c|^2\sin^2\theta}{\phi_6^2}\right]\right\} \tag{10}$$

where θ and ϕ are the polar and azimuth angles, respectively, that specify the location of the point in the spherical polar coordinate system for which the gain is to be calculated. The polar and azimuth angles specifying the radar beam axis are given by θ_c and ϕ_c, respectively. The 6 dB beamwidths, $\theta_6 = \sqrt{2}\theta_3$ and $\phi_6 = \sqrt{2}\phi_3$, specify an angular distance in a coordinate system that is fixed with respect to the radar beam axis. The quantities $|\theta-\theta_c|$ and $|\phi-\phi_c|$, however, specify angular distances in the spherical polar coordinate system. Thus, the $\sin^2\theta$ term in Equation (10) is required to convert azimuthal distances in the spherical polar coordinate system to angular distances relative to the antenna gain pattern. The dimensionless parameter G_f is included to improve the fit of this Gaussian model to real antenna patterns.

The peak gain on the radar beam axis is given by G_s. The decrease in peak gain caused by scanning the beam off boresight is given by Billetter [8] as

$$G_s = G_b(\cos\gamma_c)^{1.5} \tag{11}$$

where G_b is the gain along the antenna boresight and $\gamma_c = \cos^{-1}(\hat{r}_c \bullet \hat{r}_b)$ is the scan angle. The unit vector $\hat{r}_c$ specifies the direction of the centre of the resolution volume, hence γ_c is given by

$$\gamma_c = \cos^{-1}(\sin\theta_c\sin\phi_c\cos\psi_c\sin\phi_b + \sin\theta_c\cos\phi_c\cos\psi_c\cos\phi_b + \cos\theta_c\sin\psi_c) \tag{12}$$

Thus, the loss in peak gain is a function of the magnitude of the scan angle and not a function of the direction of this scan angle, even though the antenna array is elliptical. This approach implicitly assumes that the radiation patterns of the individual elements that make up the antenna array are circularly symmetric.

The broadening of the beam due to scanning, however, is a function of effective aperture reduction (see Billetter [8]), which is direction dependent. Thus, the increases in θ_6 and ϕ_6 caused by scanning off boresight are calculated separately as

$$\theta_6 = \frac{\theta_{6b}}{\cos\left(\frac{\pi}{2}-\psi_c-\theta_c\right)}$$
$$\phi_6 = \frac{\phi_{6b}}{\cos(\phi_b-\phi_c)} \tag{13}$$

where the 6 dB beamwidths on boresight, θ_{6b} and ϕ_{6b}, are required input parameters that are specified as single values or as sets of frequency dependent values. In the case where a frequency dependent set is used, (e.g., $\{\theta_{6b}\}$ = {3.2°, 3.0°, 2.8°, 2.6°, 2.4°, 2.2°, 2.0°} for

$\{f_t\}$ = {8.5 GHz, 9.0 GHz, 9.5 GHz, 10.0 GHz, 10.5 GHz, 11.0 GHz, 11.5 GHz}) the beamwidth values for a specific transmitted frequency are calculated by linear interpolation within the sets.

The gain along the antenna boresight, G_b, is also dependent upon the transmitted frequency, f_t, (see Doviak and Zrnić [6]), i.e.,

$$G_b = \frac{4\pi A_e f_t^2}{c^2} \tag{14}$$

where A_e is the effective area of the antenna. The input parameters G_b' and f_g (see Table 2), which specify the boresight gain for a particular frequency, can be used to calculate A_e via Equation (14). Thus, the boresight gain for arbitrary transmitted frequencies is calculated as

$$G_b(f_t) = G_b' \frac{f_t^2}{f_g^2} \tag{15}$$

As was the case for the range weighting function, the current version of the weather clutter simulation has been upgraded from that described in Thomson [1] to use this model for the antenna gain pattern.

4.5 Scan pattern

The modelled radar electronically scans in azimuth only. The azimuth extent of the scanned area is given by $\Delta\phi_s$. Figure 6 depicts how this azimuth interval is observed by a set of overlapping radar beams that adhere to the phased array model outlined in Section 4.4.

The number of required beams, N_{beam}, is determined by dividing $\Delta\phi_s$ with the smallest 3 dB beamwidth on boresight that is associated with the defined waveform set, i.e.,

$$N_{beam} = \mathbf{int}\left[\frac{\Delta\phi_s}{\mathbf{min}\left(\frac{\{\phi_{6b}\}}{\sqrt{2}}\right)} + 0.5\right] \tag{16}$$

where **int** takes the integer of its argument, **min** takes the minimum of its argument, and $\{\phi_{3b}\} = \{\phi_{6b}\}/\sqrt{2}$ represents the set of 3 dB beamwidths.

The azimuth positions of the beams are set by spacing their beam axes apart by $\mathbf{min}\{\phi_{3b}\}$. The beams are transmitted in order of increasing beam axis azimuth. Calculation of the received signal samples, however, is only performed for the particular beam in which the target is approaching (e.g., the yellow shaded beam in Figure 6). The other beams are considered only for determining the time delay between measurements along the beam containing the target (see Section 5.1).

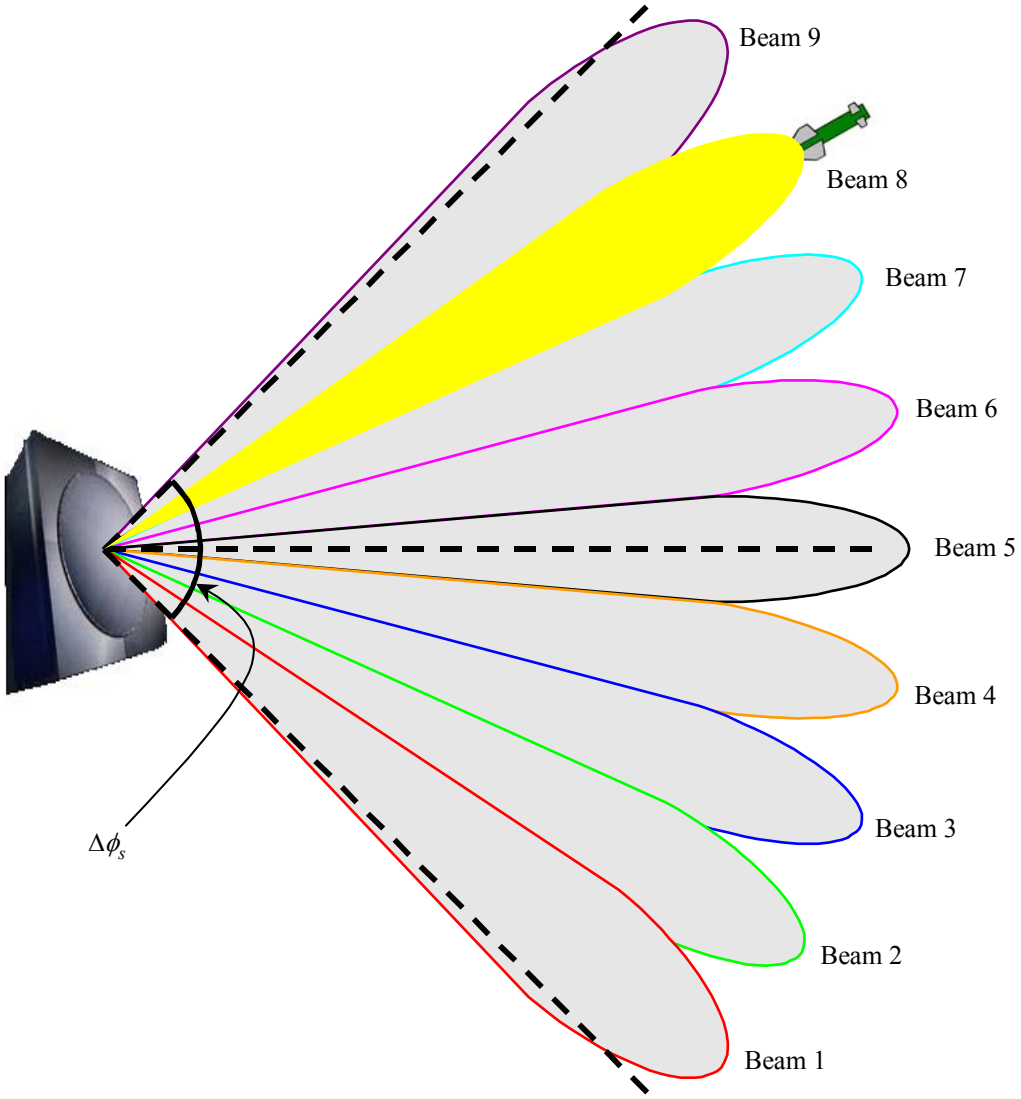

Figure 6. *Azimuthal scan pattern. The depicted 3 dB beamwidth on boresight is 10°. The azimuth extent of the scan area is 90°. The dashed lines show the boundaries of the scan area and the antenna azimuth boresight. Grey shaded regions depict the individual beams. The beam for which radar signals are calculated is shaded yellow.*

5 Missile Model

5.1 Trajectory

The modelled missile flies at a constant height above sea level and at a constant velocity directly toward the radar. The input parameters required to define the missile properties are given in Table 3. The trajectory of the missile is defined in terms of a set of points, $\vec{r}_t = (r_t, \theta_t, \phi_t)$, that define the location of the missile each time it is illuminated by a radar pulse. To calculate these points the ranges, a_t, along the missile trajectory are first determined.

Figure 7 depicts the geometry of the missile trajectory. The radar antenna is located at the origin of the *y* and *z* axes. The starting range of the missile, r_s, is a required input parameter of the target simulation. The distance along the missile trajectory from the starting point to the point where the missile trajectory intercepts the *z* axis is given by

$$a_s = (R_e + h_t)\beta_s \tag{17}$$

where R_e is the effective earth radius and h_t is the height of the missile above sea level. The angle β_s can be related to r_s using the law of cosines, i.e.,

$$r_s^2 = (R_e + h_t)^2 + (R_e + h_a)^2 - 2(R_e + h_t)(R_e + h_a)\cos\beta_s \tag{18}$$

where h_a is the height of the radar antenna above sea level. Thus, a_s can be written in terms of known quantities as

$$a_s = (R_e + h_t)\cos^{-1}\left[\frac{(R_e + h_t)^2 + (R_e + h_a)^2 - r_s^2}{2(R_e + h_t)(R_e + h_a)}\right] \tag{19}$$

The scenario is considered to end when the missile reaches the range, $r_{ec} = c\tau/2$, where eclipsing begins. Here τ is the uncompressed pulse width. The range along the flight path

Table 3. *Parameters describing the target.*

SYMBOL	EXAMPLE VALUE	DESCRIPTION
N/A	3	Swerling target type
σ_b	0.01 m^2	backscatter cross-section
v_t	281 m s^{-1}	target speed
h_t	20 m	height of target above sea level
ϕ_s	131.17324°	azimuth of target trajectory
r_s	30901.541 m	target start range

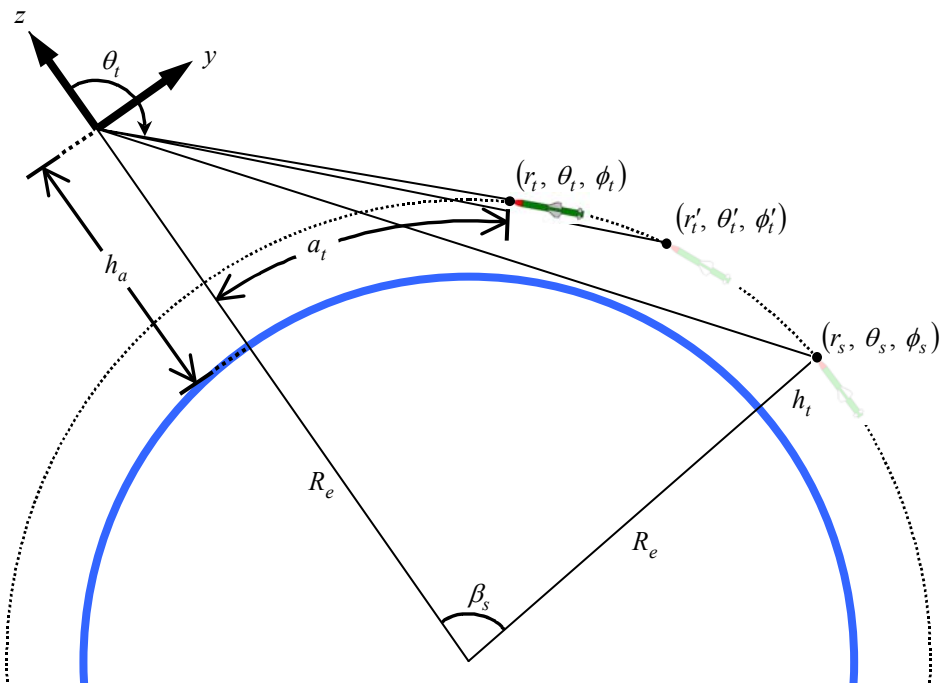

Figure 7. *Geometry of the missile trajectory. The radar antenna is located at the origin of the y and z axes. The thick blue curve represents the surface of the sea.*

from the z axis to r_{ec} is calculated similarly to a_s, i.e.,

$$a_{ec} = (R_e + h_t)\cos^{-1}\left[\frac{(R_e + h_t)^2 + (R_e + h_a)^2 - r_{ec}^2}{2(R_e + h_t)(R_e + h_a)}\right] \tag{20}$$

The first radar pulse of the scenario is transmitted along azimuth ϕ_s when the missile is at position $\vec{r}_s$ or at range a_s along the flight path. Therefore, the number of complete scans over the azimuth interval $\Delta\phi_s$ that the radar will perform during the scenario, or equivalently the number of transmitted dwells, N_d, is given by

$$N_d = \mathbf{int}\left(\frac{a_s - a_{ec}}{\mathrm{v}_t N_{beam} \sum_{p=0}^{N_d-1} \sum_{q=0}^{N_b-1} T_{spq}\, N_{cpq}}\right) + 1 \tag{21}$$

where v_t is the missile speed, p is an index that is used to sum over the individual dwells of the scenario, q is an index that is used to sum over the individual bursts of a dwell, T_{spq} is the pulse repetition time for the q^{th} burst of the p^{th} dwell, and N_{cpq} is the number of coherent pulses in the q^{th} burst of the p^{th} dwell. Equation (21) indicates that each dwell waveform is transmitted along all azimuths until the scan is complete, at which time the dwell waveform is changed to the next defined waveform.

The transmission time of the first pulse of the scenario is set to $t_{000} = 0.0$ s. The processing power of the radar system is assumed to be great enough such that there are no delays between transmitted bursts or dwells, i.e., the transmission times are completely determined by the defined n_c and T_s values. Thus, the transmission times of all subsequent pulses are calculated as

$$t_{kmn} = N_{beam} \sum_{p=0}^{k} \sum_{q=0}^{N_b-1} \left(T_{spq} \, N_{cpq} \right) - N_{beam} \sum_{q=0}^{N_b-1} \left(T_{skq} \, N_{ckq} \right) + \sum_{q=0}^{m} \left(T_{skq} \, N_{ckq} \right) - T_{skm} \, N_{ckm} + n T_{skm}$$

$$n = 0, 1, \ldots, N_{ckm} - 1$$
$$m = 0, 1, \ldots, N_b - 1 \qquad (22)$$
$$k = 0, 1, \ldots, N_d - 1$$

Here t_{kmn} is the transmission time for the n^{th} pulse of the m^{th} burst of the k^{th} dwell. The missile positions along the flight path at the time each pulse is transmitted, $a_t'(t_{kmn})$, are then calculated as

$$a_t'(t_{kmn}) = a_s - \mathrm{v}_t \, t_{kmn} \qquad (23)$$

The transmitted pulses will intercept the missile at ranges $a_t(t_{kmn})$ such that

$$a_t(t_{kmn}) = a_t'(t_{kmn}) - \mathrm{v}_t \, \Delta t_{kmn} \qquad (24)$$

where Δt_{kmn} are the times required for the transmitted pulses to travel from the antenna to the missile at ranges $r_t(t_{kmn})$. Using the law of cosines, Equation (24), and $\beta_t = a_t / (R_e + h_t)$, $r_t(t_{kmn})$ can be written as

$$r_t(t_{kmn}) = \left\{ (R_e + h_t)^2 + (R_e + h_a)^2 - 2(R_e + h_t)(R_e + h_a) \cos \left[\frac{a_t'(t_{kmn}) - \mathrm{v}_t \, \Delta t_{kmn}}{R_e + h_t} \right] \right\}^{1/2} \qquad (25)$$

The ranges to the missile positions, as defined by Equation (25), are also equal to $c \, \Delta t_{kmn}$, where c is the speed of light. Thus, the remaining unknowns in Equation (25), Δt_{kmn}, are determined by numerically solving the transcendental equations that are formed by equating the right hand side of Equation (25) to $c \, \Delta t_{kmn}$. Substituting the resultant Δt_{kmn} values back into Equation (25) will allow the ranges required for calculating the received power (see Section 5.2) to be determined.

Once the $r_t(t_{kmn})$ have been calculated the law of cosines is again used to calculate the polar angles of the missile positions at the times that the missile is illuminated, i.e.,

$$\theta_t = \pi - \cos^{-1}\left[\frac{r_t^2 + (R_e + h_t)^2 + (R_e + h_a)^2}{2r_t(R_e + h_a)}\right] \tag{26}$$

The azimuth of the flight path is constant, thus $\phi_t = \phi_s$ for all t_{kmn}.

5.2 I and Q signal samples

The radar pulses of the transmitted waveform have been grouped into bursts and dwells. The missile positions corresponding to these pulses are also grouped together according to the bursts and dwells of the transmitted waveform. Depending upon its speed and initial position, the missile may move across more than one range bin during the time required to transmit a burst. In addition, the measurement ray may be defined such that adjacent range bins overlap. Thus, for each burst, time series of I and Q signal samples must be calculated for all range bins that contain at least one missile position associated with the burst.

Figure 8 depicts an example scenario in which the missile positions of the burst affect more than one range bin. In this example the adjacent range bins overlap and the missile is moving fast enough to move across two range bins. The m^{th} burst of the k^{th} dwell has only four radar pulses ($N_{ckm} = 4$) and consequently only four corresponding missile positions. These four positions span across range bins A and B (shaded yellow), which are defined by their 6 dB resolution volumes. Thus, two sets of I and Q time series will be calculated for this burst. However, since the calculations only consider contributions to the signal samples from targets within the 6 dB resolution volume, $I_4 = Q_4 = 0$ for the time series corresponding to range bin A, and $I_1 = Q_1 = I_2 = Q_2 = 0$ for the time series corresponding to range bin B. Therefore, the average power received from the burst is likely to be greater for the time series of range bin A than that for range bin B even though range bin A is further in range.

The components of an individual complex signal sample corresponding to a given missile position and a given range bin, are calculated as

$$\begin{aligned} \mathrm{I} &= \sqrt{P_r}\cos\varphi \\ \mathrm{Q} &= \sqrt{P_r}\sin\varphi \end{aligned} \tag{27}$$

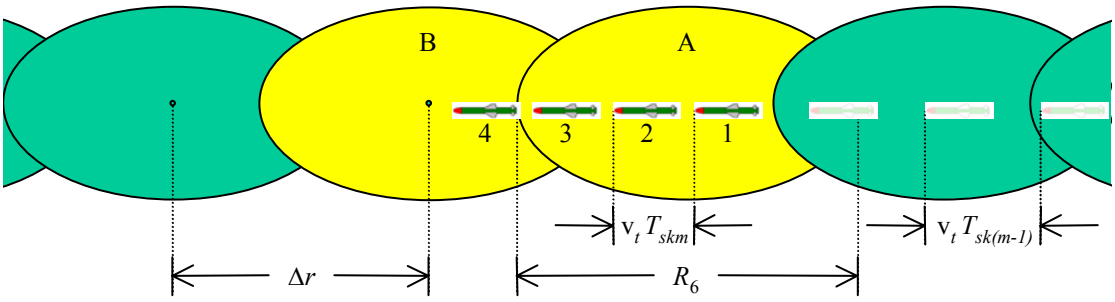

Figure 8. *Example of burst missile positions relative to the radar resolution volumes.*

where P_r is the power received from the missile, and φ is the phase difference between the radar reference signal and the received voltage sample. For simplicity, the subscripts denoting the dwell, burst, and pulse have been omitted. Equation (27) assumes that the resistance of the radar receiver is 1 Ω.

The phase of the reference signal at time t_{000} = 0.0 s is assumed to be equal to zero. Thus, the value of φ that represents the relative phase of a particular I and Q pair is calculated as

$$\varphi = \frac{-4\pi\, r_t}{\lambda} \tag{28}$$

where r_t is the corresponding missile range, and λ is the transmitted wavelength of the burst for which the I and Q time series are being calculated.

The calculation of the received power, P_r, corresponding to a particular I and Q pair, is based upon the integral form of the radar equation that was used in Thomson [1] (see also Doviak and Zrnić [6]). The power received from a collection of scatterers within the range bin centred at $\vec{r}_c = (r_c, \theta_c, \phi_c)$ is determined by integrating the weighted reflectivity field over the 6 dB resolution volume, υ, i.e.,

$$P_r(\vec{r}_c) = \int_{\upsilon} \eta(\vec{r})\, Y(\vec{r}, \vec{r}_c)\, \mathrm{d}\upsilon \tag{29}$$

where η describes the reflectivity field, and Y is a composite weighting function dependent upon the transmit/receive characteristics of the radar system. In the target simulation, however, there is only one point scatterer located at position $\vec{r}_t$. Thus, the reflectivity field is given by

$$\eta(\vec{r}) = \sigma_b \delta(\vec{r} - \vec{r}_t) = \frac{\sigma_b\, \delta(r - r_t)\, \delta(\theta - \theta_t)\, \delta(\phi - \phi_t)}{r_t^2 \sin\theta_t} \tag{30}$$

where $\delta(\vec{r} - \vec{r}_t)$ is the Dirac delta function defined by (see Jordan and Balmain [9])

$$\int_{\upsilon} \delta(\vec{r} - \vec{r}_t)\, \mathrm{d}\upsilon \;\; = \begin{cases} 1 & \text{if } \vec{r}_t \text{ is in } \upsilon \\ 0 & \text{if } \vec{r}_t \text{ is not in } \upsilon \end{cases} \tag{31}$$

The backscatter cross section of the target, σ_b, is an input parameter required by the simulation. However, its value is set to zero for all target positions that are below the radar horizon, i.e., for target positions such that

$$\theta_t > \pi/2$$

$$(R_e + h_a)\sin(\pi - \theta_t) \le R_e \tag{32}$$

$$r_t \ge \ell_s$$

where ℓ_s is the distance from the radar antenna to the sea surface along the path through the earth to the missile position (see Figure 9). By applying the law of cosines to the left triangle shown in Figure 9, ℓ_s can be written as

$$\ell_s = \left[R_e^2 + (R_e + h_a)^2 - 2R_e(R_e + h_a)\sin(\theta_t - \psi_g)\right]^{1/2} \tag{33}$$

The grazing angle ψ_g is calculated by applying the law of sines to the left triangle of Figure 9, i.e.,

$$\psi_g = \frac{\pi}{2} - \sin^{-1}\left[\left(\frac{R_e + h_a}{R_e}\right)\sin(\pi - \theta_t)\right] \tag{34}$$

Substituting Equation (30) into Equation (29) gives

$$P_r(\vec{r}_c) = \int_{\upsilon} \sigma_b\, \delta(\vec{r} - \vec{r}_t)\, Y(\vec{r}, \vec{r}_c)\, \mathrm{d}\upsilon \quad = \sigma_b\, Y(\vec{r}_t, \vec{r}_c) \tag{35}$$

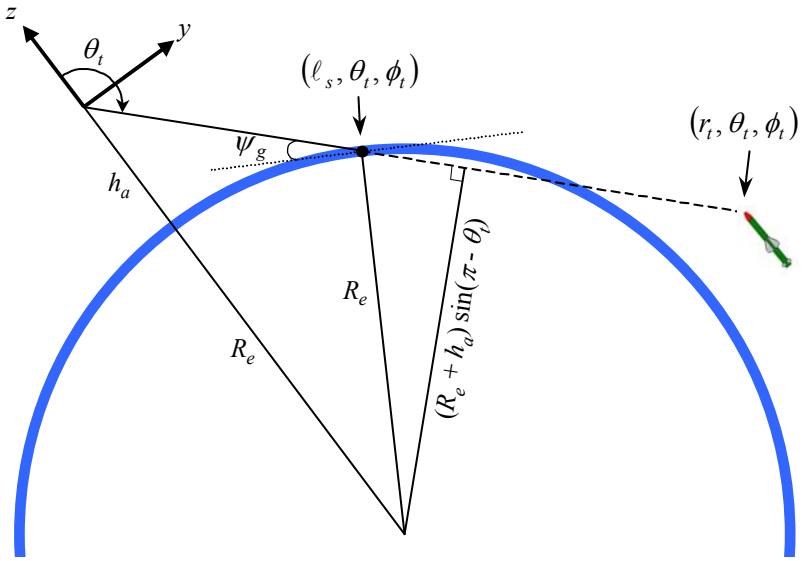

Figure 9. *Geometry describing target positions below the radar horizon. The thick blue curve represents the sea surface.*

when $\vec{r}_t$ is within υ. Expansion of the composite weighting function (Thomson [1], Doviak and Zrnic [6]) gives a form of the radar equation for a point target that allows the position of the target within the resolution volume, and its corresponding weighting by the antenna gain pattern and the radar receiver, to be considered, i.e.,

$$P_r(\vec{r}_c) = \frac{P_c P_t \lambda^2 G_{sys} G^2(\theta_t, \phi_t, \theta_c, \phi_c) W^2(r_t, r_c) \sigma_b}{(4\pi)^3 L_a(r_t, \theta_t, \phi_t) r_t^4} \tag{36}$$

where P_t is the transmitted power, and G_{sys} is the receiver system gain. Note that a term, L_r, was incorrectly included in the composite weighting function of Thomson [1] to describe a power loss due to finite receiver bandwidth. This term is not necessary when the range weighting function is included in the composite weighting function. Hence L_r does not appear in Equation (36) and is no longer a parameter of the weather clutter simulation (Thomson [1]). The factor P_c has been included to model the increase in power backscattered from a coherent target when pulse compression is used. The 2-way attenuation of the radar signal over the path from the antenna to the target and back, $L_a(r_t, \theta_t, \phi_t)$, is calculated using the empirical formulas described in Thomson [1].

5.3 Multipath interference

Refraction of the radar signals in the atmosphere has been accounted for by using an effective earth radius in all calculations. This approach allows the signal ray paths to be considered as straight lines, which simplifies the calculations required to determine the interference effects caused by a reflective sea surface. In this case, the radar signal will travel along four different paths to the target and back to the antenna. These paths are shown in Figure 10.

The calculations described in Section 5.2 apply to the signals received along path 1. The I and Q signals samples corresponding to paths 2, 3, and 4 are calculated in a similar way, except for adjustments related to the reflection coefficient, the path length, the phase shift upon reflection, and the divergence of the radar beam caused by reflection from a spherical surface.

Path 3 involves a reflection of the radar signal from the sea surface both on the way to the target and on the way back. For both reflections the signal is reflected from a medium (sea) that is more optically dense than the medium in which it is travelling (air). Therefore, each

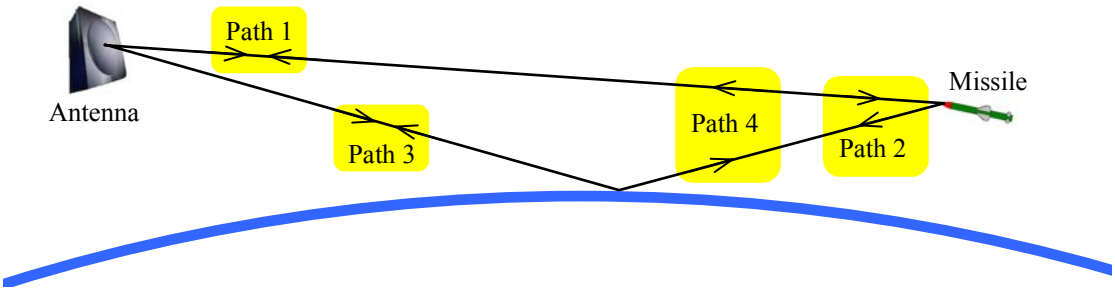

Figure 10. *The signal paths that cause interference. The thick blue curve represents the sea surface.*

reflection will result in a phase shift of π radians. Consequently, the phase of the received signal can be calculated as in Equation (28), i.e.,

$$\varphi_3 = \frac{-4\pi\, r_{t3}}{\lambda} \tag{37}$$

where $r_{t3} = \ell_{t3i} + \ell_{t3r}$ is the range along path 3. Figure 11 defines the quantities ℓ_{t3i} and ℓ_{t3r} as the range from the antenna to the reflection point and the range from the reflection point to the target, respectively.

The power received from the target along path 3 is calculated using the radar equation, i.e.,

$$P_{r3}(\vec{r}_c) = \frac{\rho^2 P_c P_t\, \lambda^2\, G_{sys}\, G^2(\theta_{t3}, \phi_t, \theta_c, \phi_c)\, W^2(r_{t3}, r_c)\, \sigma_b}{(4\pi)^3 L_a(r_{t3}, \theta_{t3}, \phi_t)\, r_{t3}^4} \tag{38}$$

However, in this case the received power will be reduced based upon the reflectance of the sea surface, ρ. In addition, the composite weighting function must be evaluated at the polar angle that specifies the direction of the reflection point, θ_{t3}, and at the range r_{t3}.

The calculation of ρ, ℓ_{t3i}, ℓ_{t3r}, and θ_{t3} in the target simulation is done in a very similar way to that described for the weather clutter simulation in Thomson [1]. The main difference between the two calculations is the divergence factor. These calculations are reproduced in Annex A of this report because of this difference and also because of differences in notation.

The I and Q components corresponding to signals received along path 3 are calculated as

$$\begin{aligned} \mathrm{I}_{3n} &= \sqrt{P_{r3n}}\, \cos\varphi_{3n} \\ \mathrm{Q}_{3n} &= \sqrt{P_{r3n}}\, \sin\varphi_{3n} \end{aligned} \tag{39}$$

In Equation (39), the subscript "3" refers to path 3 and the subscript "*n*" refers to the individual signal samples of a received burst as in Section 2.

Signal path 2 involves only one reflection from the sea surface. Thus, a phase shift of π radians must be added to the phase calculation, i.e.,

$$\varphi_2 = \pi - \frac{4\pi\, r_{t2}}{\lambda} \tag{40}$$

where the apparent range is calculated as $r_{t2} = (r_t + r_{t3})/2$. The single reflection is also represented in the power calculation as a factor of ρ, i.e.,

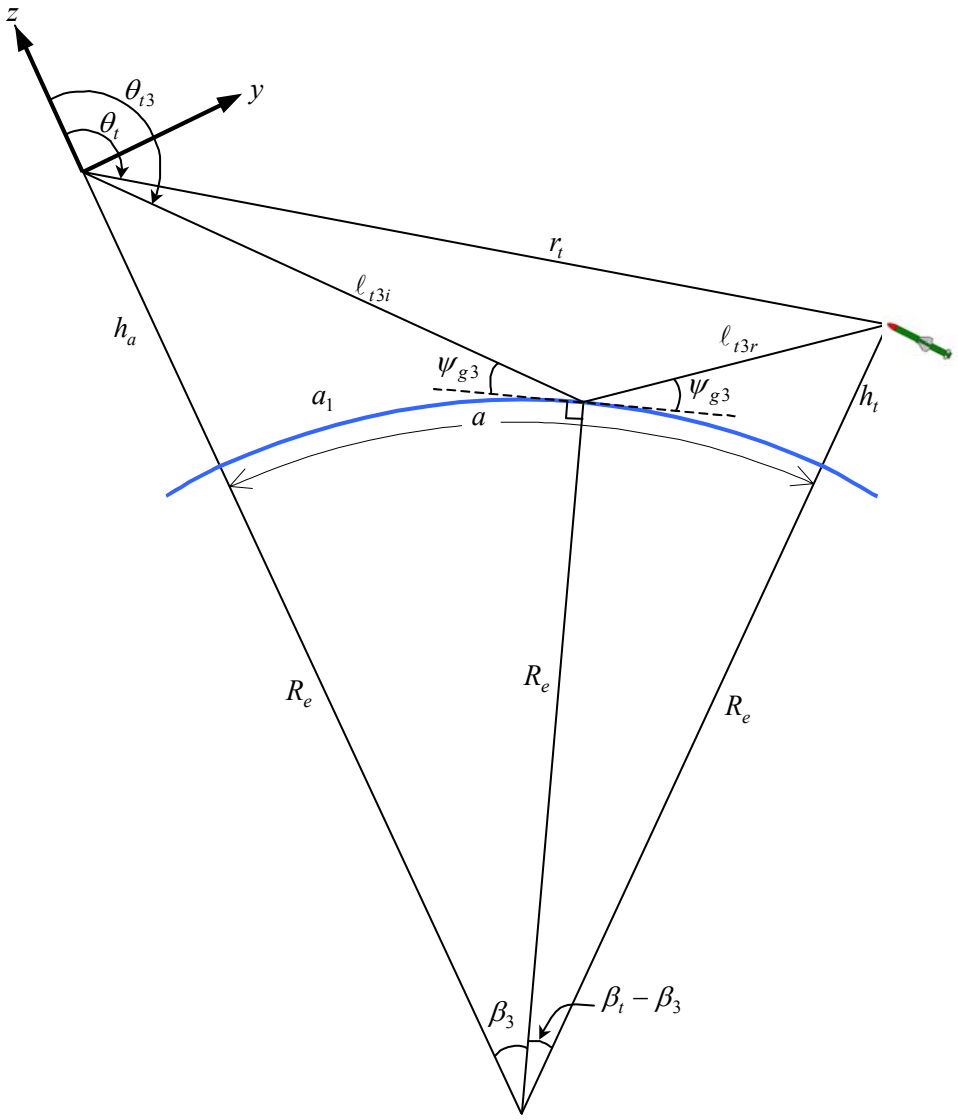

Figure 11. *Path 3 geometry.*

$$P_{r2}(\bar{r}_c) = \frac{\rho\, P_c P_t\, \lambda^2\, G_{sys}\, G_2^2\, W^2(r_{t2}, r_c)\, \sigma_b}{(4\pi)^3\, L_{a2}\, r_{t2}^4} \tag{41}$$

In this case the apparent gain corresponding to path 2, G_2, is calculated as

$$G_2 = \sqrt{G(\theta_t, \phi_t, \theta_c, \phi_c)\; G(\theta_{t3}, \phi_t, \theta_c, \phi_c)} \tag{42}$$

and the apparent 2-way attenuation corresponding to path 2, L_{a2}, is calculated as

$$L_{a2} = \frac{L_a(r_t, \theta_t, \phi_t) + L_a(r_{t3}, \theta_{t3}, \phi_t)}{2} \tag{43}$$

The I and Q samples corresponding to signal path 4 are exactly the same as those for signal path 2. Hence, the path 2 and 4 signal samples are given by

$$\begin{aligned} \mathrm{I}_{4n} &= \mathrm{I}_{2n} = \sqrt{P_{r2n}} \cos\varphi_{2n} \\ \mathrm{Q}_{4n} &= \mathrm{Q}_{2n} = \sqrt{P_{r2n}} \sin\varphi_{2n} \end{aligned} \tag{44}$$

Once the signal samples have been calculated for the four different paths, the overall received signal samples for a given burst and a given range bin are calculated by coherent summation, i.e.,

$$\begin{aligned} \mathrm{I}_n &= \mathrm{I}_{1n} + \mathrm{I}_{2n} + \mathrm{I}_{3n} + \mathrm{I}_{4n} \\ \mathrm{Q}_n &= \mathrm{Q}_{1n} + \mathrm{Q}_{2n} + \mathrm{Q}_{3n} + \mathrm{Q}_{4n} \end{aligned} \tag{45}$$

As shown in Figure 8, the received pulses corresponding to a particular burst can contribute backscattered power to the signal samples corresponding to more than one range bin. In general, it is possible that the set of range bins associated with a given burst may not be the same for all of the different signal paths because of their differing path lengths. The target simulation properly considers these range differences when summing the multipath signal samples for each range bin.

6 Statistical Model

As shown in Figure 2 the statistical model creates random numbers that will be filtered by the output of the missile model. These random numbers represent the fluctuations in the received radar signal that are caused by the interference, at the antenna port, of the waves backscattered from the different scattering centres of the target. The statistical model can generate random numbers appropriate for targets that have the properties of the four Swerling models (see Skolnik [5], p. 2.21). The Swerling target type is specified as an input parameter of the target simulation (see Table 3).

6.1 Statistical fluctuations for Swerling 1 Targets

The Swerling 1 model describes a target whose received signal voltage fluctuates slowly from scan to scan according to a Rayleigh probability density function. This model can be used to describe a target with many scattering centres of equal radar cross section. The relative positions of these scattering centres with respect to the radar do not change significantly over the time period of the pulse repetition interval, but do change significantly over the time period between consecutive dwells (i.e., the scan time).

A random number, representing a statistical fluctuation, is calculated for all of the I and Q values generated for the entire scenario. The individual signal samples are represented as $\mathrm{I}_{\alpha\beta n}$ and $\mathrm{Q}_{\alpha\beta n}$ where $\alpha = 0, 1, 2, \ldots, N_b N_d - 1$ is an index that represents the transmitted burst of the scenario, β is an index that represents the range bins that are simultaneously affected by the received signals corresponding to a particular burst, and $n = 0, 1, 2, \ldots, N_{c\alpha} - 1$ is an index representing the pulses in a burst.

In the Swerling 1 case four zero-mean Gaussian random numbers are generated for each complex signal sample as

$$\begin{aligned} \mathrm{f}_{\alpha\beta n} &= \frac{x_\alpha}{\sqrt{2}} \\ \mathrm{f}'_{\alpha\beta n} &= \frac{x'_\alpha}{\sqrt{2}} \\ \mathrm{f}''_{\alpha\beta n} &= \frac{x''_\alpha}{\sqrt{2}} \\ \mathrm{f}'''_{\alpha\beta n} &= \frac{x'''_\alpha}{\sqrt{2}} \end{aligned} \tag{46}$$

where the x_α, x'_α, x''_α, x'''_α are Gaussian distributed random numbers having a mean of zero and a standard deviation of one. Fluctuations corresponding directly to the I and Q values are then calculated as

$$\begin{aligned} \mathrm{f}^{\mathrm{I}}_{\alpha\beta n} &= \left[\left(\mathrm{f}_{\alpha\beta n}\right)^2 + \left(\mathrm{f}'_{\alpha\beta n}\right)^2\right]^{-1/2} \cos\left[\tan^{-1}\left(\frac{\mathrm{f}'''_{\alpha\beta n}}{\mathrm{f}''_{\alpha\beta n}}\right)\right] = \mathrm{f}''_{\alpha\beta n}\left[\frac{\left(\mathrm{f}_{\alpha\beta n}\right)^2 + \left(\mathrm{f}'_{\alpha\beta n}\right)^2}{\left(\mathrm{f}''_{\alpha\beta n}\right)^2 + \left(\mathrm{f}'''_{\alpha\beta n}\right)^2}\right]^{1/2} \\ \mathrm{f}^{\mathrm{Q}}_{\alpha\beta n} &= \left[\left(\mathrm{f}_{\alpha\beta n}\right)^2 + \left(\mathrm{f}'_{\alpha\beta n}\right)^2\right]^{-1/2} \sin\left[\tan^{-1}\left(\frac{\mathrm{f}'''_{\alpha\beta n}}{\mathrm{f}''_{\alpha\beta n}}\right)\right] = \mathrm{f}'''_{\alpha\beta n}\left[\frac{\left(\mathrm{f}_{\alpha\beta n}\right)^2 + \left(\mathrm{f}'_{\alpha\beta n}\right)^2}{\left(\mathrm{f}''_{\alpha\beta n}\right)^2 + \left(\mathrm{f}'''_{\alpha\beta n}\right)^2}\right]^{1/2} \end{aligned} \tag{47}$$

This approach ensures that the fluctuations corresponding to the quadrature samples are 90° out of phase with the fluctuations corresponding to the in-phase samples.

Equation (46) specifies that for a given α, $\mathrm{f}_{\alpha\beta n}$ is the same for all β and n. That is, for any given burst, the value of the random number representing the fluctuations is the same for all I and Q values in all range bins affected by the returns corresponding to that particular burst. The fluctuation for the n^{th} signal sample in each range bin affected by a particular burst must be the same since the target motion will be insignificant over the time period between range samples, i.e., the time required for the radar signal to travel the distance of the range resolution.

The fluctuations calculated using Equation (47) are appropriate for a Swerling 1 target that is viewed by a multiple burst waveform in which the transmitted frequencies change from burst to burst. In this case the signal voltage received by the target will fluctuate faster than the rate that is defined for a Swerling 1 target. This is because the interference of the waves backscattered from the scattering centres will vary as a function of the transmitted frequency.

In general, the target simulation does not require the frequency to change from burst to burst. Thus, for a Swerling 1 target, the random fluctuations that are calculated in Equation (47) must be adjusted if the frequency remains constant for any two consecutive bursts of a dwell. Consequently, for each dwell the frequency of burst 0 is first compared with the frequency of burst 1. If they are the same then the random fluctuations, $\mathrm{f}^{\mathrm{I}}_{\alpha\beta n}$ and $\mathrm{f}^{\mathrm{Q}}_{\alpha\beta n}$, corresponding to burst 1 are set equal to those corresponding to burst 0. Next the frequencies of burst 1 and 2 are compared. If they are equal, the $\mathrm{f}^{\mathrm{I}}_{\alpha\beta n}$ and $\mathrm{f}^{\mathrm{Q}}_{\alpha\beta n}$ for burst 2 are set equal to those for burst 1. This process is continued until, finally, the frequencies of burst $\left(N_b - 2\right)$ and $\left(N_b - 1\right)$ are compared. If they are equal, the $\mathrm{f}^{\mathrm{I}}_{\alpha\beta n}$ and $\mathrm{f}^{\mathrm{Q}}_{\alpha\beta n}$ for burst $\left(N_b - 1\right)$ are set equal to those for burst $\left(N_b - 2\right)$.

Fluctuations corresponding to the power spectral coefficients are calculated as

$$\mathrm{f}^{S}_{\alpha\beta i} = \left(\mathrm{f}^{\mathrm{I}}_{\alpha\beta i}\right)^2 + \left(\mathrm{f}^{\mathrm{Q}}_{\alpha\beta i}\right)^2 \qquad i = n = 0, 1, 2, \ldots, N_c - 1 \tag{48}$$

where the index *n*, used in the time domain, has been replaced with *i*, which is used in the frequency domain to represent the coefficients of the power and phase spectra. The $\mathrm{f}^{S}_{\alpha\beta i}$ are exponentially distributed random numbers having a mean of one. These values are then filtered with the output of the missile model (see Figure 2 and Equation (4)). A mean value of one ensures that the filtering process does not alter the power of the signal that is output by the missile model.

As stated in Section 2, the phase spectrum of the final signal for a Swerling 1 target is taken directly from the output of the missile model. Hence, the statistical model does not calculate phase fluctuations in this case.

6.2 Statistical fluctuations for Swerling 2 Targets

The Swerling 2 model describes a target whose received signal voltage fluctuates rapidly from pulse to pulse according to a Rayleigh probability density function. As in the case of the Swerling 1 target, this model is used to describe a target with many scattering centres of equal radar cross section. However, in this case the relative positions of the scattering centres with respect to the radar do change significantly over the time period of the pulse repetition interval.

For a Swerling 2 target the statistical model generates four random numbers for each complex signal sample, i.e.,

$$\begin{aligned}
\mathrm{f}_{\alpha\beta n} &= x_{\alpha n}\sqrt{\frac{N_{c\alpha}}{2}} \\
\mathrm{f}'_{\alpha\beta n} &= x'_{\alpha n}\sqrt{\frac{N_{c\alpha}}{2}} \\
\mathrm{f}''_{\alpha\beta n} &= x''_{\alpha n}\sqrt{\frac{N_{c\alpha}}{2}} \\
\mathrm{f}'''_{\alpha\beta n} &= x'''_{\alpha n}\sqrt{\frac{N_{c\alpha}}{2}}
\end{aligned} \tag{49}$$

where the $x_{\alpha n}$, $x'_{\alpha n}$, $x''_{\alpha n}$, $x'''_{\alpha n}$ are Gaussian distributed random numbers having a mean of zero and a standard deviation of one. The fluctuations corresponding to the I and Q signal samples are then calculated using Equation (47). In this case the resulting $\mathrm{f}^{\mathrm{I}}_{\alpha\beta n}$ and $\mathrm{f}^{\mathrm{Q}}_{\alpha\beta n}$ are zero-mean Gaussian random numbers having a standard deviation of $\sqrt{N_{c\alpha}/2}$.

Equation (49) specifies that unique random numbers are generated for each signal sample of each burst. However, as in the case of a Swerling 1 target, the random numbers are the same, for any particular signal sample, for each of the multiple range bins that are simultaneously affected by the returns from any one burst.

Fluctuations corresponding to the coefficients of the power and phase spectra are calculated by **DFT**, i.e., for each α (burst) and for each β (range bin) the fluctuations are calculated as

$$\mathrm{f}_i^S = \left(\mathbf{Re}\left\{\mathrm{f}_i^{\mathrm{X}}\right\}\right)^2 + \left(\mathbf{Im}\left\{\mathrm{f}_i^{\mathrm{X}}\right\}\right)^2 \qquad \mathrm{f}_i^{\Phi} = \tan^{-1}\left(\frac{\mathbf{Im}\left\{\mathrm{f}_i^{\mathrm{X}}\right\}}{\mathbf{Re}\left\{\mathrm{f}_i^{\mathrm{X}}\right\}}\right) \tag{50}$$

where

$$\begin{aligned}
\vec{\mathrm{f}}^{\mathrm{X}} &= \left(\mathrm{f}_0^{\mathrm{X}}, \mathrm{f}_1^{\mathrm{X}}, \mathrm{f}_2^{\mathrm{X}}, \ldots, \mathrm{f}_{N_c-1}^{\mathrm{X}}\right) = \mathbf{DFT}\left\{\vec{\mathrm{f}}^{\mathrm{I}} + j\,\vec{\mathrm{f}}^{\mathrm{Q}}\right\} \\
\vec{\mathrm{f}}^{\mathrm{I}} &= \left(\mathrm{f}_0^{\mathrm{I}}, \mathrm{f}_1^{\mathrm{I}}, \mathrm{f}_2^{\mathrm{I}}, \ldots, \mathrm{f}_{N_c-1}^{\mathrm{I}}\right) \\
\vec{\mathrm{f}}^{\mathrm{Q}} &= \left(\mathrm{f}_0^{\mathrm{Q}}, \mathrm{f}_1^{\mathrm{Q}}, \mathrm{f}_2^{\mathrm{Q}}, \ldots, \mathrm{f}_{N_c-1}^{\mathrm{Q}}\right)
\end{aligned} \tag{51}$$

The power spectral fluctuations, $\mathrm{f}_{\alpha\beta i}^S$, will be exponentially distributed random numbers having a mean of one if the **DFT** is defined with the following normalization

$$\begin{aligned}
\mathrm{F}(u) &= \frac{1}{N_c}\sum_{y=0}^{N_c-1}\mathrm{f}(y)\exp\left(-j2\pi u\,y/N_c\right) \\
\mathrm{f}(y) &= \sum_{u=0}^{N_c-1}\mathrm{F}(u)\exp\left(-j2\pi u\,y/N_c\right)
\end{aligned} \tag{52}$$

The power spectral fluctuations are used to filter the output of the missile model (see Equation (4)). The phase fluctuations, $\mathrm{f}_{\alpha\beta i}^{\Phi}$, will be random numbers uniformly distributed between $-\pi$ and π. For a Swerling 2 target these numbers are used directly as the coefficients of the phase spectra.

6.3 Statistical fluctuations for Swerling 3 Targets

The Swerling 3 model describes a target whose received signal voltage fluctuates slowly from scan to scan according to a χ^2 distribution of degree 4 (see Nathanson [10], p. 167). This model can be used to describe a target that consists of one dominant scattering centre and many other scattering centres of smaller radar cross section. The relative positions of these scattering centres with respect to the radar do not change significantly over the time period of the pulse repetition interval, but do change significantly over the time period between consecutive dwells.

For a Swerling 3 target the statistical model generates the individual fluctuations corresponding to the power spectral coefficients as

$$\mathrm{f}_{\alpha\beta i}^{S} = \frac{1}{4}\left[\left(x_{\alpha}\right)^{2} + \left(x'_{\alpha}\right)^{2} + \left(x''_{\alpha}\right)^{2} + \left(x'''_{\alpha}\right)^{2}\right] \tag{53}$$

where the x_{α}, x'_{α}, x''_{α}, x'''_{α} are again Gaussian distributed random numbers having a mean of zero and a standard deviation of one. The resulting, $\mathrm{f}_{\alpha\beta i}^{S}$, are degree 4 χ^2 distributed random numbers having a mean of one.

Equation (53) specifies that a unique random number is generated for each burst. As in the case of a Swerling 1 target, these numbers must be adjusted if the transmitted frequency is the same for any two consecutive bursts of a dwell. Once the $\mathrm{f}_{\alpha\beta i}^{S}$ have been appropriately adjusted (see Section 6.1), they are used to filter the spectral power coefficients that are output by the missile model (see Equation (4)).

As in the case of a Swerling 1 target, no fluctuations are generated for the coefficients of the phase spectra corresponding to a Swerling 3 target.

6.4 Statistical fluctuations for Swerling 4 Targets

The Swerling 4 model describes a target whose received signal voltage fluctuates rapidly from pulse to pulse according to a χ^2 distribution of degree 4. As in the case of the Swerling 3 target, this model can be used to describe a target that consists of one dominant scattering centre and many other scattering centres of smaller radar cross section. However, in this case the relative positions of the scattering centres with respect to the radar do change significantly over the time period of the pulse repetition interval.

The individual fluctuations, $\mathrm{f}_{\alpha\beta i}^{S}$, corresponding to the power spectral coefficients corresponding to a Swerling 4 target are calculated as

$$\mathrm{f}_{\alpha\beta i}^{S} = \frac{1}{4}\left[\left(x_{\alpha i}\right)^{2} + \left(x'_{\alpha i}\right)^{2} + \left(x''_{\alpha i}\right)^{2} + \left(x'''_{\alpha i}\right)^{2}\right] \tag{54}$$

In this case, unique random numbers are generated for each spectral coefficient of each burst. These χ^2 distributed numbers (mean of one) are then used to filter the output of the missile model (see Equation (4)).

The fluctuations that will represent the coefficients of the phase spectra are calculated as

$$\mathrm{f}_{\alpha\beta i}^{\Phi} = 2\pi\, \mathrm{U}_{\alpha i} - \pi \tag{55}$$

where the $\mathrm{U}_{\alpha i}$ are random numbers uniformly distributed between zero and one.

7 Example Output

This section presents example data generated by the target simulation. The data are presented in the form of comparisons that are intended to demonstrate the simulation's ability to generate realistic target signals. Specifically, example output generated by the target simulation are compared in terms of propagation factor and received power with the outputs of TERPEM (TERrain Parabolic Equation Model) and ADAPT_MFR (ADAPTive MultiFuntion Radar Simulation), respectively.

"TERPEM is a propagation modelling tool for assessing the effects of atmospheric refraction and terrain diffraction on radar and communications systems in the frequency range 30 MHz to 100 GHz" [11]. Since the time of writing of reference [11] the lower frequency limit of TERPEM has been extended to 1 MHz (Levy and Craig [12]). As part of the work to extend TERPEM's capabilities, the TERPEM output was evaluated against the output generated by GRWAVE (Ground-WAVE propagation program, Gill [13]). Excellent agreement between the outputs of the two codes was achieved (Levy and Craig [12]). The calculations performed by GRWAVE are based upon the theory of Rotheram, [14, 15], which represents a completely different approach to propagation calculations than that used by TERPEM. The TERPEM output has also been compared with the output of MLAYER. Again, excellent agreement was achieved [M. Levy, private communication]. MLAYER was developed by the Naval Ocean Systems Centre for calculating the signal levels of electromagnetic waves propagating in a multilayer tropospheric waveguide environment over sea water (Yeoh [16]). This software is based upon a full mode solution to Maxwell's equations and is often used as a baseline for testing propagation calculations. Good agreement has also been achieved (Thomson [17]) between the output of TERPEM and the outputs of AREPS (Advanced Refractive Effects Prediction System, Patterson [18]) and NEMESiS (Naval ElectroMagnetic Environment SImulation System). Both of these codes use parabolic equation methods similar to those used in TERPEM. NEMESiS is based upon the approach presented by Barrios [19]. Thus, TERPEM is considered to be accurate for the conditions of interest and to represent a good standard for evaluation of the target simulation in terms of propagation factor.

The pattern propagation factor, F, is defined "as the ratio of the field strength that is actually present at a point in space to that which would be present if free-space propagation had occurred with the antenna beam directed toward the point in question" (Long [20], p 111). In terms of the notation used in this report, the TERPEM propagation factor calculations consider the radar equation to take the following form

$$P_r = \frac{P_t\, G_{sys}\, G_f^2\, G_s^2\, \lambda^2\, \sigma_b}{(4\pi)^3\, r^4}\, F_T^4 \tag{56}$$

where P_r is the power received from a single radar pulse that is backscattered by a target at range r. By this definition F_T^4 includes the angular dependence of the antenna gain function.

The propagation factor is calculated from the output I and Q data generated by the target simulation by first determining the received power as a function of range. An average received power for a particular range bin is calculated as

$$\overline{P}_r(r_c) = \frac{1}{N_c} \sum_{n=0}^{N_c-1} \left(\mathrm{I}_n^2 + \mathrm{Q}_n^2 \right) \tag{57}$$

A propagation factor value, F^4, corresponding to this range bin is then calculated by substituting Equation (57) into Equation (56), i.e.,

$$F^4(r_c) = \frac{(4\pi)^3 \, \overline{P}_r \, r_c^4}{P_t \, G_{sys} \, G_f^2 \, G_s^2 \, \lambda^2 \, \sigma_b} \tag{58}$$

These calculations have been performed for the scenario defined in Tables 1, 2, and 3. The resulting propagation factor values (scaled by P_c) are shown as the green curve in Figure 12. However, it is expected that these F^4 values will not agree well with the F_T^4 values calculated by TERPEM (blue curve of Figure 12) because of differences in the form of the radar equation used by TERPEM and the target simulation.

The free space (path 1) radar equation used by the target simulation can be written as

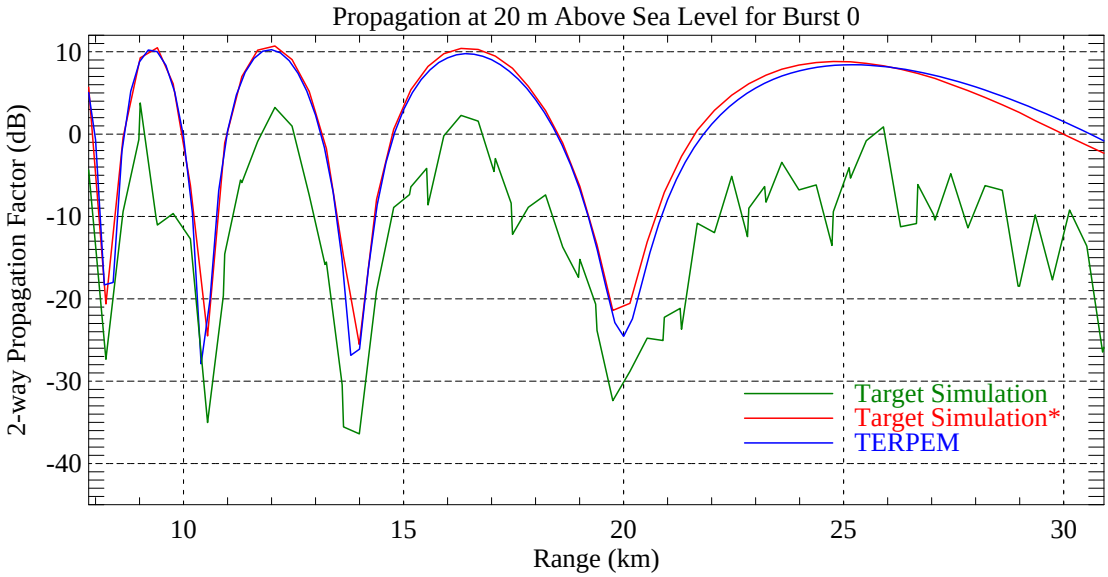

Figure 12. *Comparison of the propagation factors calculated by the target simulation and TERPEM. The modelled scenario is represented by the parameters listed in Tables* ***1****,* ***2****, and* ***3****. The T_s, f_t, and N_c parameters for this case represent burst 0 of a four burst dwell that is repeated continuously throughout the flight time of the missile. The blue curve shows F_T^4 vs. range. The red curve shows F'^4 vs. range. The green curve shows F^4/P_c vs. range.*

$$P_r(\vec{r}_c) = \frac{P_c P_t \lambda^2 G_{sys} G_f^2 G_s^2 G_N^2(\theta_t, \phi_t, \theta_c, \phi_c) W^2(r_t, r_c) \sigma_b}{(4\pi)^3 L_a(r_t, \theta_t, \phi_t) r_t^4} \tag{59}$$

where $G_N^2(\theta_t, \phi_t, \theta_c, \phi_c) = G^2 / (G_f^2 G_s^2)$ is the normalized antenna gain pattern. This equation determines the power, corresponding to a range bin at $\vec{r}_c$, that is received from a single transmitted pulse. The presence of the earth can be incorporated into this radar equation by adding a pattern propagation factor, which gives

$$P_r(\vec{r}_c) = \frac{P_c P_t \lambda^2 G_{sys} G_f^2 G_s^2 W^2(r_t, r_c) \sigma_b}{(4\pi)^3 L_a(r_t, \theta_t, \phi_t) r_t^4} F^4 \tag{60}$$

Thus, propagation factor values calculated using Equations (57) and (58) would incorporate the effects of pulse compression, attenuation by precipitation, and range weighting, which are not considered by TERPEM. Therefore, to achieve a better comparison, the scenario defined by Tables 1, 2, and 3 is executed by the target simulation again, with the attenuation and range weighting calculations switched off. In addition, since TERPEM only performs calculations in a two dimensional plane (range and height), the input parameter of the target simulation describing the target azimuth is set equal to the azimuth of the radar beam axis ($\phi_s = \phi_c = 130°$). TERPEM also does not consider statistical fluctuations. Hence, the Swerling number input parameter is set to zero, which corresponds to no statistical fluctuations. Using these considerations, average received powers, $\overline{P}_r'$, are calculated from the I' and Q' outputs as

$$\overline{P}_r'(r_c) = \frac{1}{P_c N_c} \sum_{n=0}^{N_c-1} \left[(\mathrm{I}_n')^2 + (\mathrm{Q}_n')^2 \right] \tag{61}$$

A propagation factor value , F'^4, that is comparable with that produced by TERPEM is then calculated for each range bin as

$$F'^4(r_c) = \frac{(4\pi)^3 \overline{P}_r' r_c^4}{P_t G_{sys} G_f^2 G_s^2 \lambda^2 \sigma_b} \tag{62}$$

The red curve plotted in Figure 12 shows the range dependence of these F'^4 values. Agreement to within 3 dB of the F_T^4 values produced by TERPEM (blue curve) is now achieved at all range bins, even in the multipath nulls.

The waveform parameters, T_s, f_t, and N_c corresponding to the case of Figure 12 (see Table 2) describe one burst of a four burst dwell waveform. The target simulation generated the plotted data by transmitting this dwell waveform repeatedly throughout the flight time of the missile. The waveform parameters describing all four bursts of the dwell are shown in Table 4. Similar comparison plots between the propagation factors calculated by TERPEM and those derived from the target simulation for bursts 1, 2, and 3 are shown in Figures 13, 14,

Table 4. *Waveform parameters.*

BURST NUMBER	T_S (µs)	f_t (GHz)	N_c
0	240.7	10.93	26
1	221.5	10.65	29
2	212.8	9.74	33
3	206.4	8.955	37

and 15. Similarly good agreement between the target simulation and TERPEM is achieved for each burst.

As stated in Section 2, the target simulation will not correctly calculate the propagation of the radar signal into the "intermediate region". Blake [4] (p. 279) gives quantitative expressions, based on grazing angle, that approximate the region of validity of the geometrical optics approach used in the target simulation. However, these expressions are not exact. A better method of testing whether or not the geometrical optics approach is valid may be to compare the calculated results with those of TERPEM as has been done in Figures 12, 13, 14, and 15. In these cases the target simulation agrees well with TERPEM and can be considered accurate.

Figure 16 shows an example for which the target simulation becomes inaccurate. In this case, the parameters corresponding to Figure 15 have been used except for the antenna height, which has been lowered to 5 m. Lowering the antenna height causes the radar horizon to decrease. Thus, the target simulation calculations extend into the intermediate region. The propagation factor calculated by the target simulation now deviates from that calculated by TERPEM at far ranges. Therefore, the target simulation calculations should only be used, for

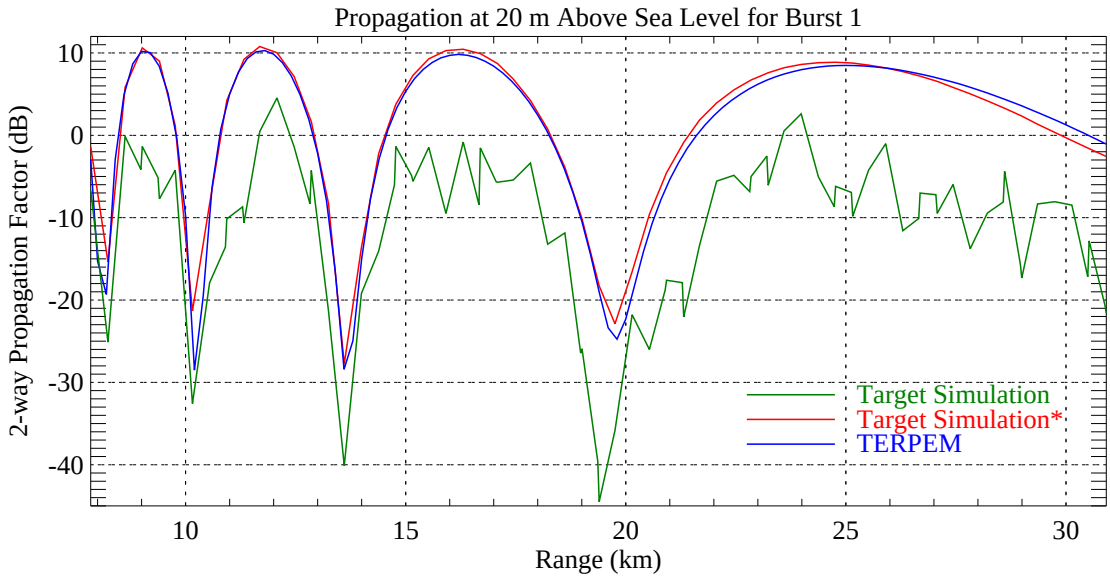

Figure 13. *Comparison of the propagation factors calculated by the target simulation and TERPEM. The target simulation data corresponds to the burst 1 waveform parameters. The blue curve shows* F_T^4 *vs. range. The red curve shows* F'^4 *vs. range. The green curve shows* F^4/P_c *vs. range.*

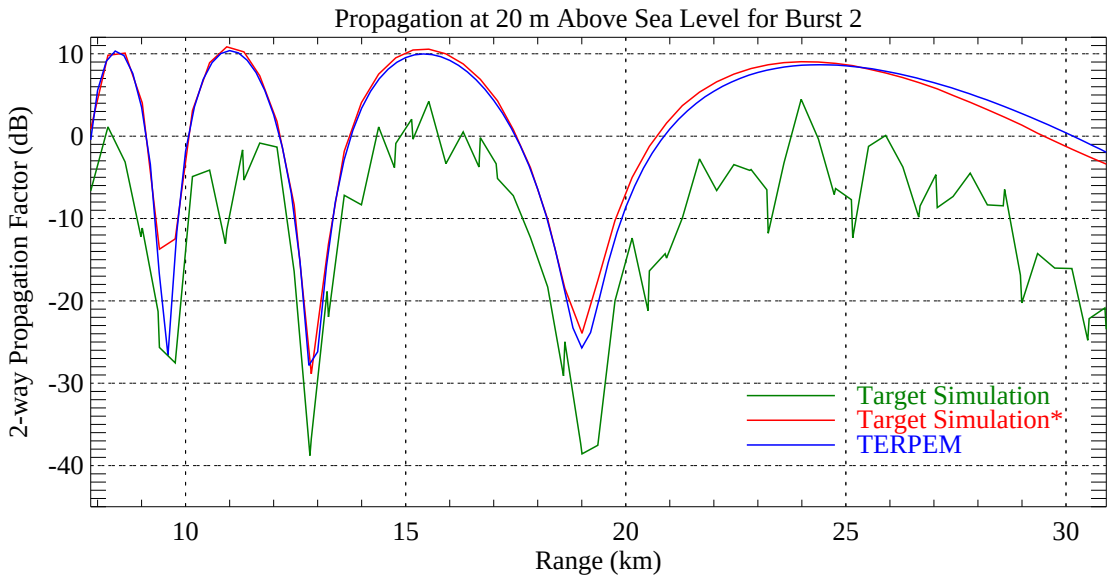

Figure 14. *Comparison of the propagation factors calculated by the target simulation and TERPEM. The target simulation data corresponds to the burst 2 waveform parameters. The blue curve shows* F_T^4 *vs. range. The red curve shows* F'^4 *vs. range. The green curve shows* F^4/P_c *vs. range.*

the case of Figure 16, at ranges less than ~ 22.5 km. This method of assessing the accuracy of the geometrical optics approach used in the target simulation, i.e., comparison with TERPEM, leads to the obvious recommendation that the target simulation should be upgraded to use TERPEM for propagation calculations.

ADAPT_MFR is the latest in a line of comprehensive computer programs (developed under contract for the Defence R&D Canada – Ottawa) designed to evaluate the detection capability of multifunction radars when operating against anti-ship missiles (Gauthier et al. [21], Gauthier [22]). The simulated scenarios can include up to five missiles (sea skimmers or high divers) and up to five collocated multifunction radars operating simultaneously in littoral regions in the presence of jamming. These radars are optimized for horizon search but can perform any user-defined search pattern, including cueing, confirmation and tracking. As a consequence of the larger scope of the modelled scenarios, relative to the target simulation, the ADAPT_MFR calculations are performed with lower fidelity, e.g., the simulation does not calculate the complex components of the received signal voltage. It does, however, calculate the received target powers as a function of range using TERPEM output for the propagation factor. Since these calculations are performed in a different manner than those of the target simulation, a favourable comparison between the two simulation outputs should increase confidence in the accuracy of the outputs produced by both simulators.

The burst 0 target power as calculated by the target simulation using the parameters of Tables 1, 2, and 3 is plotted as a function of range (green curve) in Figure 17. The target power as calculated by ADAPT_MFR using equivalent parameters is also plotted (blue curve) in Figure 17. As was the case for the propagation factor comparisons of Figures 12, 13, 14, and 15, the main difference between these two curves can be accounted for by factors that are not considered by both simulations. In this case, ADAPT_MFR only calculates the mean target power. Statistical fluctuations of the received target power are only considered in the

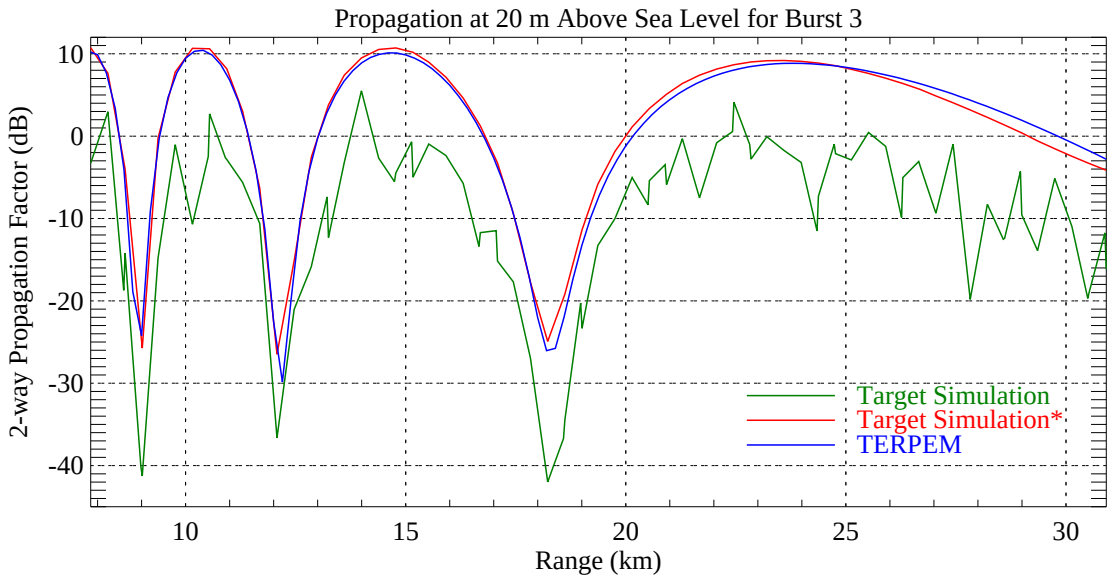

Figure 15. *Comparison of the propagation factors calculated by the target simulation and TERPEM. The target simulation data corresponds to the burst 3 waveform parameters. The blue curve shows* F_T^4 *vs. range. The red curve shows* F'^4 *vs. range. The green curve shows* F^4/P_c *vs. range.*

probability of detection calculations. In addition, ADAPT_MFR does not explicitly consider the range weighting applied to targets at different locations within the measurement volume. Thus, the output of the target simulation is regenerated with the statistical fluctuations and range weighting calculations turned off. These adjusted data, plotted as the red curve in Figure 17, agree very well with the results calculated by ADAPT_MFR. The small differences between the adjusted data produced by the target simulation and the data produced by ADAPT_MFR for equivalent conditions are almost entirely due to the differences found between the propagation factors calculated by TERPEM and the target simulation. Similar plots corresponding to bursts 1, 2, and 3 are shown in Figures 18, 19, and 20. Similarly favourable comparisons are achieved in each case.

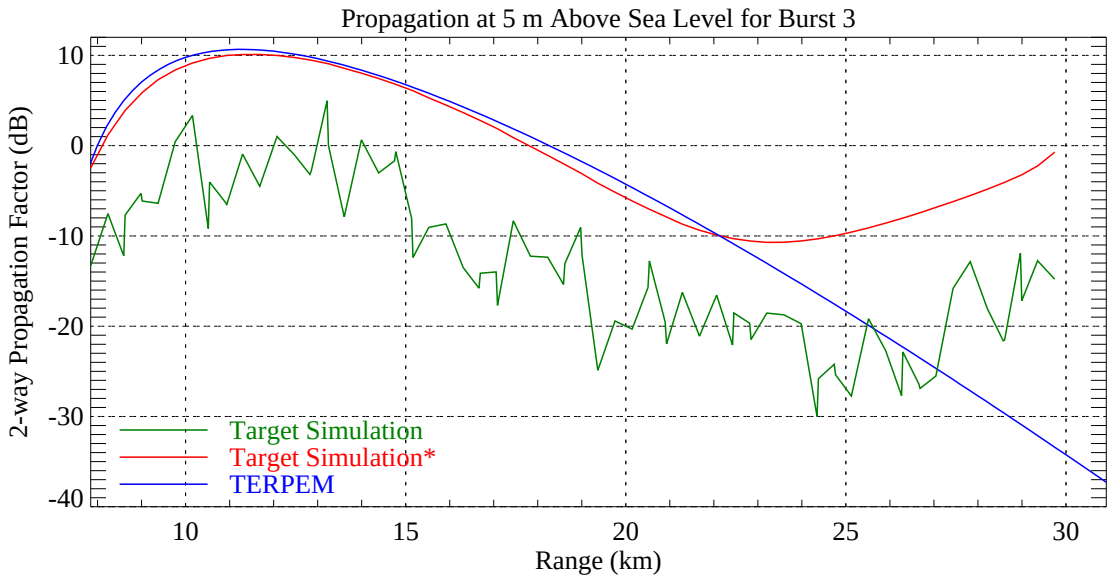

Figure 16. *Comparison of the propagation factors calculated by the target simulation and TERPEM. The parameters of the modelled scenario are the same as that corresponding to Figure* ***15****, except for antenna height, which was set to 5 m. The blue curve shows* F_T^4 *vs. range. The red curve shows* F'^4 *vs. range. The green curve shows* F^4/P_c *vs. range.*

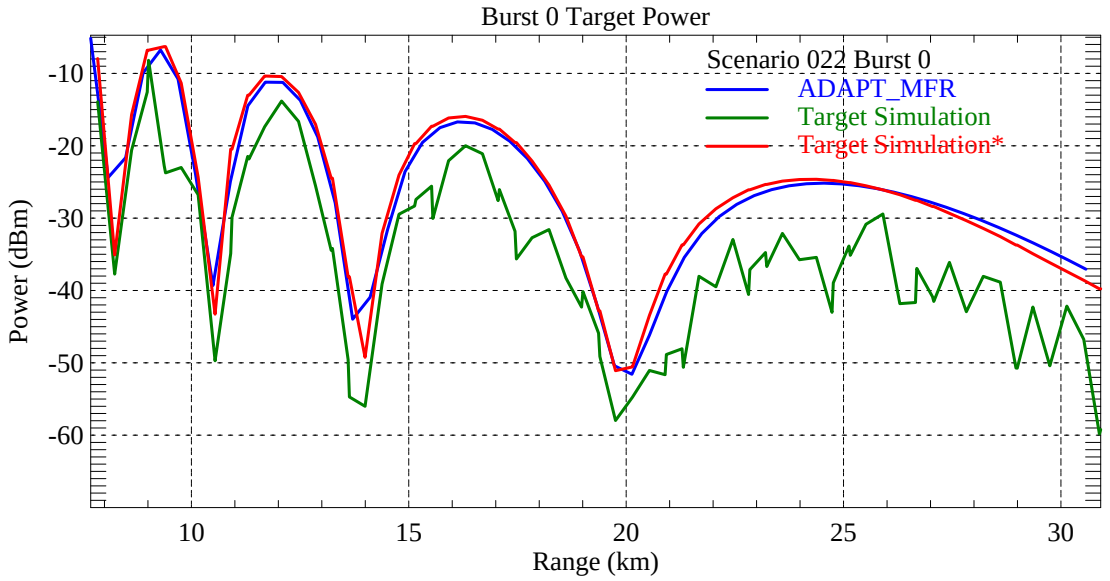

Figure 17. *Comparison of the burst 0 target powers generated by the target simulation and ADAPT_MFR for the scenario defined in Tables* ***1****,* ***2****, and* ***3****. The green curve shows the standard output of the target simulation. The red curve shows the data generated by the target simulation without range weighting or statistical fluctuations. The blue curve shows the equivalent target powers generated by ADPT_MFR.*

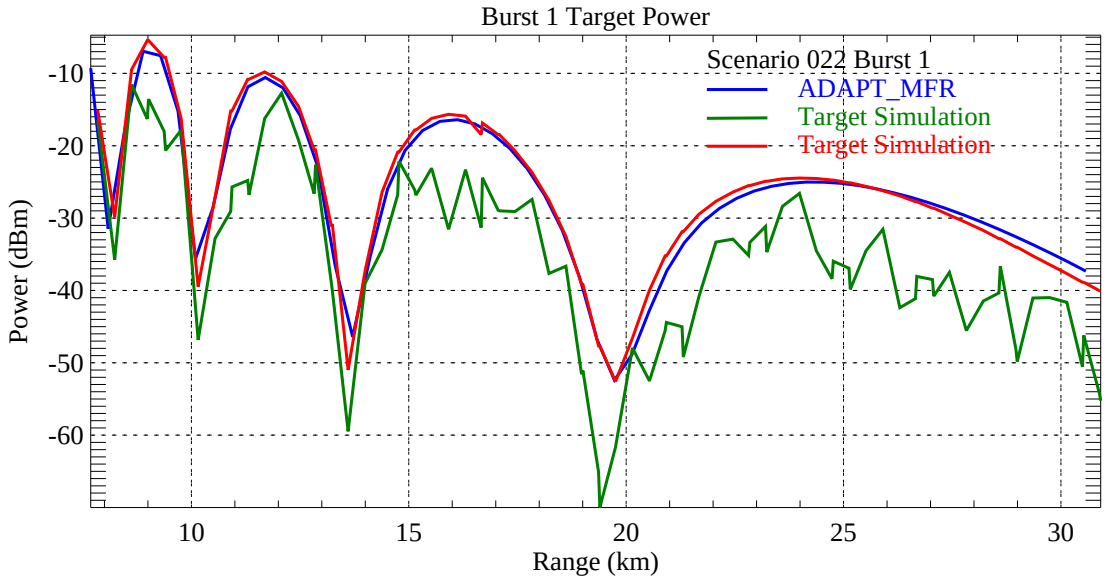

Figure 18. *Comparison of the burst 1 target powers generated by the target simulation and ADAPT_MFR for the scenario defined in Tables **1**, **2**, **3**, and **4**. The green curve shows the standard output of the target simulation. The red curve shows the data generated by the target simulation without range weighting or statistical fluctuations. The blue curve shows the equivalent target powers generated by ADPT_MFR.*

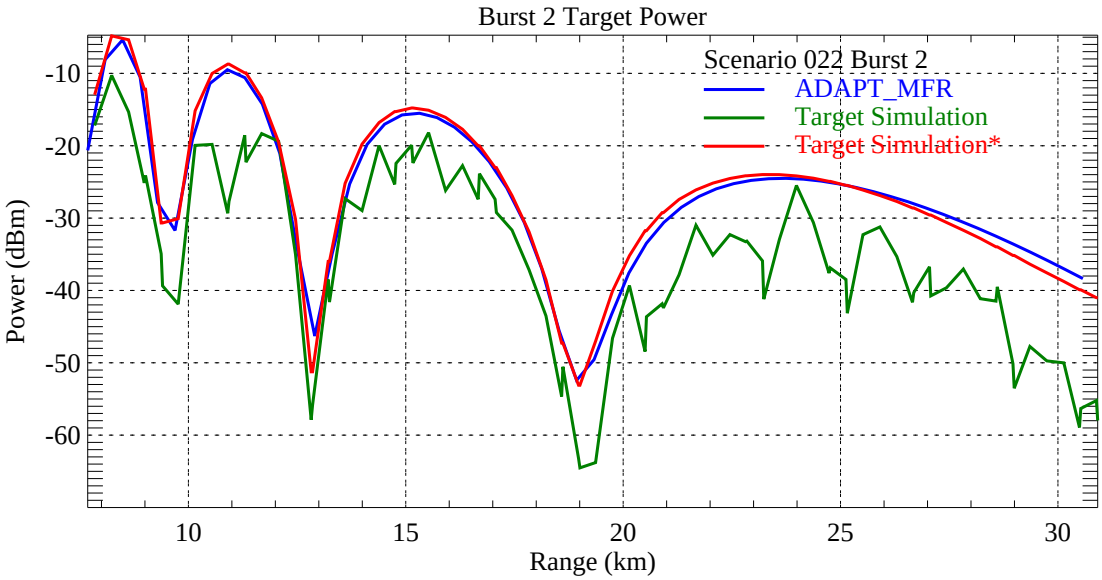

Figure 19. *Comparison of the burst 2 target powers generated by the target simulation and ADAPT_MFR for the scenario defined in Tables **1**, **2**, **3**, and **4**. The green curve shows the standard output of the target simulation. The red curve shows the data generated by the target simulation without range weighting or statistical fluctuations. The blue curve shows the equivalent target powers generated by ADPT_MFR.*

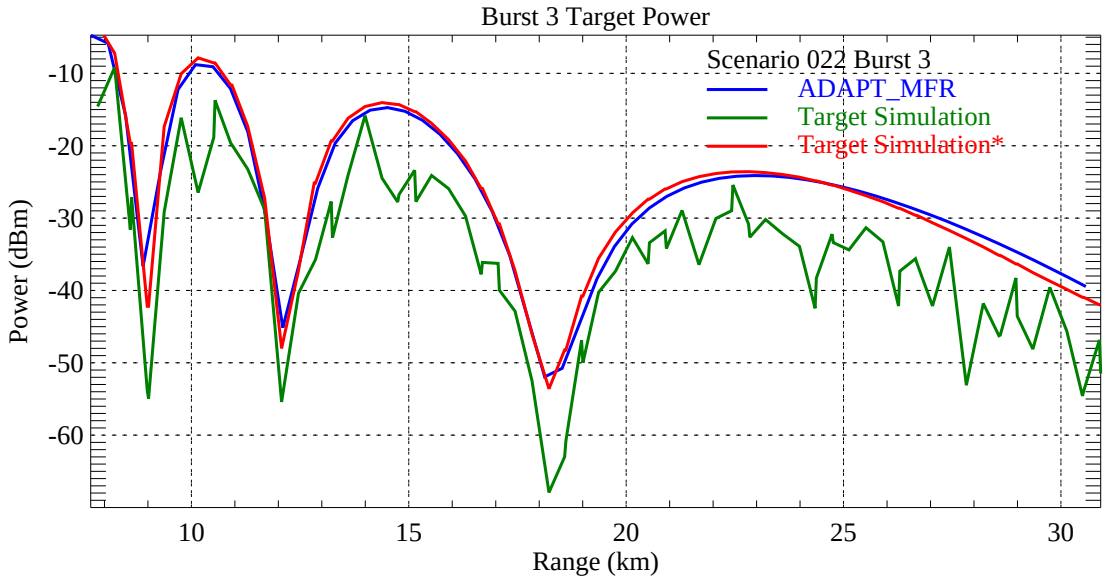

Figure 20. *Comparison of the burst 3 target powers generated by the target simulation and ADAPT_MFR for the scenario defined in Tables **1**, **2**, **3**, and **4**. The green curve shows the standard output of the target simulation. The red curve shows the data generated by the target simulation without range weighting or statistical fluctuations. The blue curve shows the equivalent target powers generated by ADPT_MFR.*

8 Summary and Conclusions

This report describes a high fidelity simulation of the complex voltage signals produced by the receiver of a shipborne horizon scanning phased array radar when observing an approaching sea-skimming anti-ship missile in adverse weather conditions. The output of this simulation is to be used together with the output of high fidelity clutter and radar signal processor simulations to investigate radar detection performance (e.g., see Thomson [3]). Weather effects are only considered in terms of attenuation of the signals received from the target. The attenuation models used limit the applicability of this simulation to radar frequencies in the X, C, or S-band.

The modelled target moves directly toward the observing radar at constant speed along a flight path of constant altitude and azimuth. The received target signals can incorporate statistical fluctuations corresponding to the any of the four Swerling target types.

The environment is modelled as a stratiform precipitation field above a rough spherical sea surface, exactly as was done in Thomson [1]. Refraction of the radar signals by the atmosphere is considered by using an effective earth radius approach. Multipath interference caused by the reflection of the radar signal by the sea surface is calculated geometrically. Diffraction effects are ignored. Thus, the applicability of this target simulation is limited to the "interference region" (see Blake [4], p 279) of atmospheres having an index of refraction that changes linearly with height.

The modelled radar system transmits a multiple burst waveform in which the frequency, pulse repetition time, and number of pulses per burst can all change from burst to burst and dwell to dwell. The motion of the target from pulse to pulse is considered. Range weighting of the target within the resolution volume is also considered. The specific forms of the range weighting and antenna gain functions used in the target simulation represent upgrades to the models used in the weather clutter simulation as described by Thomson [1]. These upgrades have now also been included in the weather clutter simulation.

The target simulation was evaluated by comparing its output in terms of pattern propagation factor and received target power with the outputs of TERPEM [11] and ADAPT_MFR (Gauthier et al. [21]; Gauthier [22], respectively. Good agreement was achieved in each case, except where the calculations were extended beyond the interference region into the intermediate region. To increase the applicability of this simulation it is recommended that it be integrated with TERPEM so that propagation can be correctly considered at any range in any atmospheric structure. Nevertheless, the favourable comparisons in the interference region demonstrate that this simulation is accurate, where applicable, and that it can be used with confidence for its stated purpose of assessing radar detection performance. In addition, the good agreement between the target simulation and ADAPT_MFR allows further comparisons to be made between the two simulations, e.g., in terms of probability of detection, with the knowledge that potential differences are not due to modelling of the power received from the target.

9 References

1. Thomson, A. D. (1999). Simulation of weather clutter as measured by an X-band phased array radar. (DREO TR 1999-077). Defence Research Establishment Ottawa.

2. Jones, G., Nohara, T. J., and Premji, A. (2001). Modification to an adaptive multifunction radar simulator. (DREO, PWGSC Contract No. W7714-000370/001/SV). Sicom Systems Limited.

3. Thomson, A. D., Unpublished Report.

4. Blake, L. V. (1986). Radar range-performance analysis. Artech House, Inc., p 443.

5. Skolnik, M. I. (1990). Radar Handbook. 2nd ed. McGraw-Hill Inc..

6. Doviak, R. J., and Zrnić, D. S. (1993). Doppler radar and weather observations. 2nd ed. Academic Press, Inc., San Diego, p 562.

7. Barton, D. K. (1976). Radar system Analysis. Artech House Inc., p 608.

8. Billetter, D. R. (1989). Multifunction array radar. Artech House, Inc., p 189.

9. Jordan, E. C., and Balmain, K. G. (1968). Electromagnetic waves and radiating systems. 2nd ed. Prentice-Hall, Inc., Englewood Cliffs, New Jersey, p 753.

10. Nathanson, F. E. (1991). Radar design principles. 2nd ed. McGraw-Hill, Inc., p 720.

11. TERPEM user guide (1998). Signal Science Limited, 20 Alexander Close, Abingdon, Oxon, OX13 1XA, U.K..

12. Levy, M.F., and Craig, K. H. (2001). HF extension of TERPEM. (DREO CR 2001-121) (DREO, PWGSC Contract No. W7714-010484/A-GBL). Signal Science Limited.

13. Gill, R. S. (1985). Ground-wave propagation program. GEC Research Laboratories, Marconi Research Centre, West Hanningfield Road, Great Baddow, Chelmsford, Essex, CM2 8HN.

14. Rotheram, S. (1981). Ground wave propagation, I: Theory for short distances. *IEE Proc.*, part F, 128(5), 275-284.

15. Rotheram, S. (1981). Ground wave propagation, II: Theory for medium and long distances and reference propagation curves. *IEE Proc.*, part F, 128(5), 285-295.

16. Yeoh, L. (1990). An analysis of MLAYER: A multilayer tropospheric propagation program. (NPS-62-90-009; ADA232733). Naval Postgraduate School, Monterey, California, p 158.

17. Thomson, A. D. (2002). TERPEM evaluation. Presentation to *TTCP SEN TP-6* annual meeting at Defence R & D Canada – Ottawa.

18. Patterson, W. L. (1998). Advanced Refractive Effects Prediction System (AREPS): Versio 1.0 User's Manual. (Technical document 3028). Space and Naval Warfare Systems Center, San Diego, California, p 149.

19. Barrios, A. E. (1994). A terrain parabolic equation model for propagation in the troposphere. *IEEE Trans. Antennas Propag.*, 42 (1), 90-98.

20. Long, M. W. (2001). Radar reflectivity of land and sea. 3rd ed., Artech House, p 534.

21. Gauthier, S., Riseborough, E., Jones, G., Bhattacharya, T., Premji, A., Weber, P., and Nohara, T. J. (1999). Rotating multifunction array radar simulator. *NATO Workshop on" Detection and Tracking of Low Altitude Low RCS Air Vehicles"*, Copenhagen, Denmark. Available from author at Defence R & D Canada at Ottawa, 3701 Carling Avenue, Ottawa, Canada, K1A 0Z4

22. Gauthier, S. (1998). Simulation of a multifunction radar operating in horizon search mode. In *Proceedings of the infrared information symposium: Third NATO-IRIS joint symposium*, 19-31. Quebec City, Canada: NATO.

23. Hansen, J. P. (1986). A system for performing ultra high resolution backscatter measurements of splashes. In *Int. Microwave Theory and Techniques Symp.*, 633-636. Baltimore, MD.

24. Katsaros, K., and Buettner, K. J. K. (1969). Influence of rainfall on temperature and salinity of the ocean surface. *J. Appl. Meteor.*, 8, 15-18.

25. Freehafer, J. E., Fishback, W.T, Furry, W. H., and Kerr, D. E. (1987). Theory of propagation in a horizontally stratified atmosphere. In D. E. Kerr (Ed.), *Propagation of short radio waves*, pp. 27-180. London, UK: Peter Peregrinus Ltd..

26. Fowles, G. R. (1975). Introduction to Modern Optics. 2nd ed. New York: Dover Publications Inc., p 328.

27. Klein, L. A., and Swift, C. T. (1977). An improved model for the dielectric constant of sea water at microwave frequencies. *IEEE Trans. Antennas Propag.*, 25, 104-111.

Annex A: Reflectance of the Sea Surface

The reflectance describes the ratio of reflected to incident energy. This quantity must be calculated for the case of a rough spherical sea surface. Typically, the roughness of the sea is considered to be caused by wind and swell, and is characterized in terms of a sea state. However, precipitation impacts at the reflection point may also have an effect on the reflectance. There are no works known to the author that consider the effect of a precipitation disturbed sea surface on the reflected wave. Backscatter from a rain disturbed sea surface has, however, been investigated. In these studies the time history of the splash structure resulting from a raindrop impact has been investigated (Hansen 1986 [23]). Three main scattering structures have been found. These are the "crown" and "stalk" of the splash as well as the "ring waves" that propagate outward along the sea surface from the impact location. Since the crown and stalk features are above the sea surface, the resulting backscatter may be more similar to that of rain backscatter than that of sea backscatter. Therefore, in this study these features are considered to result in a negligible increase in rain rate at the sea surface, which will cause a negligible increase in attenuation of the forward-scattered wave. It is also assumed that the small-amplitude ring waves do not introduce significant additional structure to the already existing structure caused by gravity waves and capillary waves. Thus, it is assumed that disturbance of the sea surface by impacting precipitation does not significantly effect the reflectance.

Rain will also have a significant effect on the temperature and salinity of the sea surface, depending on the rain rate and duration of the rainfall (Katsaros and Buettner 1969 [24]). However, the reflectance of the sea surface is not very sensitive to changes in temperature and salinity. Therefore, this effect is also neglected in the reflectance calculations.

The reflectance, ρ, is given by the magnitude of the complex reflection coefficient, i.e.,

$$\rho = \begin{cases} |R_{\mathrm{v}}|^2 & \text{vertical polarization} \\ |R_h|^2 & \text{horizontal polarization} \end{cases} \tag{63}$$

The reflection coefficients for a rough spherical sea surface are given by Skolnik [5] (p. 2.38) as

$$\begin{aligned} R_{\mathrm{v}} &= R_{\mathrm{v}o}\, F_r\, F_D \qquad \text{vertical polarization} \\ R_h &= R_{ho}\, F_r\, F_D \qquad \text{horizontal polarization} \end{aligned} \tag{64}$$

where the $R_{\mathrm{v}o}$ and R_{ho} are the magnitudes of the smooth-flat-earth reflection coefficients for vertical and horizontal polarizations, respectively. The specular-reflection roughness factor is given by F_r, and F_D denotes the divergence factor.

Skolnik [5] (p. 2.40) gives the specular-reflection roughness factor as

$$F_r = e^{-\xi}\, \mathrm{J}_0(\mathrm{j}\xi) \tag{65}$$

where J_0 is the order zero Bessel function of the first kind and

$$\xi = 2\left(\frac{2\pi \mathrm{H}\sin\psi_{g3}}{\lambda}\right)^2 \tag{66}$$

The standard deviation of wave height, H, is parameterized in terms of a sea state parameter (see Table 5), which is a required input of the simulation.

The grazing angle, ψ_{g3}, is calculated using the path 3 geometry depicted in Figure 11. It has been shown that a cubic equation in the arc length, a_1, can be written in terms of h_a, R_e, h_t, and the arc length a (see Freehafer et al. [25], p. 113), i.e.,

$$2a_1^3 - 3aa_1^2 + \left[a^2 - 2R_e\left(h_a + h_t\right)\right] a_1 + 2R_e h_a a = 0 \tag{67}$$

The solution to Eq. (67) is given by

$$a_1 = \frac{a}{2} + q_1 \cos\left(\frac{q_2 + \pi}{3}\right) \tag{68}$$

where

$$\begin{aligned} q_1 &= \frac{2}{\sqrt{3}}\sqrt{R_e\left(h_a + h_t\right) + \left(\frac{a}{2}\right)^2} \\ q_2 &= \cos^{-1}\left[\frac{2R_e\left(h_a - h_t\right)a}{q_1^3}\right] \end{aligned} \tag{69}$$

Using the law of sines on the outer triangle of Figure 11 the arc length a can be written as

$$a = R_e \sin^{-1}\left(\frac{r_t \sin\theta_t}{R_e + h_t}\right) \tag{70}$$

Once a_1 is determined, the angle $\beta_3 = a_1 / R_e$ can be used to calculate the range to the reflection point, ℓ_{t3i}, by applying the law of cosines to the left triangle of Figure 11, i.e.,

Table 5. *Relationship of sea state to standard deviation of wave height.*

SEA STATE, H_S	H **(m)**	**SEA STATE,** H_S	H **(m)**
0	0.0	4	0.4953
1	0.0762	5	0.762
2	0.1524	6	1.2192
3	0.3048	7	2.286

$$\ell_{t3i} = \left[R_e^2 + \left(R_e + h_a\right)^2 - 2R_e\left(R_e + h_a\right)\cos\beta_3\right]^{\frac{1}{2}} \tag{71}$$

The range from the reflection point to the target is similarly calculated by applying the law of cosines to the right triangle of Figure 11, i.e.,

$$\ell_{t3r} = \left[R_e^2 + \left(R_e + h_t\right)^2 - 2R_e\left(R_e + h_t\right)\cos\left(\beta_t - \beta_3\right)\right]^{\frac{1}{2}}$$

where $\beta_t = a/R_e$. The range ℓ_{t3i} is used to calculate the polar angle of the reflection point by applying the law of sines to the left triangle, i.e.,

$$\theta_{t3} = \pi - \sin^{-1}\left(\frac{R_e \sin\beta_3}{\ell_{t3i}}\right) \tag{72}$$

Finally, the grazing angle can be determined from β_3 and θ_{t3}, i.e.,

$$\psi_{g3} = \theta_{t3} - \beta_3 - \frac{\pi}{2} \tag{73}$$

The divergence factor describes the weakening of the signal power density caused by reflection from a spherical surface. It is calculated as

$$F_D = \left[1 + \frac{2a_1\left(a - a_1\right)}{aR_e \sin\psi_{g3}}\right]^{-1/2} \tag{74}$$

Although the atmosphere was considered to be an absorbing medium for the attenuation calculations, it will be assumed to be non-absorbing when calculating the reflection coefficients. For this case, the equations of Fowles [26] (p. 166-167) can be used to write the smooth-flat-earth reflection coefficients as

$$\begin{aligned} R_{vo} &= \frac{-\mathrm{N}^2 \sin\psi_{g3} + \sqrt{\mathrm{N}^2 - \cos^2\psi_{g3}}}{\mathrm{N}^2 \sin\psi_{g3} + \sqrt{\mathrm{N}^2 - \cos^2\psi_{g3}}} \\ R_{ho} &= \frac{\sin\psi_{g3} - \sqrt{\mathrm{N}^2 - \cos^2\psi_{g3}}}{\sin\psi_{g3} + \sqrt{\mathrm{N}^2 - \cos^2\psi_{g3}}} \end{aligned} \tag{75}$$

where N is the complex index of refraction of sea water. For a non-magnetic material, $\mathrm{N} = \sqrt{\varepsilon_r}$, where ε_r is the complex dielectric constant (or relative permittivity). The complex dielectric constant for sea water is calculated using the equations of Klein and Swift [27]. The standard Debye expression gives ε_r, in F/m, as

$$\varepsilon_r = \varepsilon_\infty + \frac{\varepsilon_s - \varepsilon_\infty}{1 + \mathrm{j}2\pi\,\mathrm{f}_t\,\tau_r} - \frac{\mathrm{j}\sigma}{2\pi\,\mathrm{f}_t\,\varepsilon_o} \tag{76}$$

where ε_∞ is the dielectric constant at infinite frequency, ε_s is the static dielectric constant, f_t is the transmitted radar frequency, τ_r is the relaxation time, and σ is the ionic conductivity. Klein and Swift [27] state that choosing $\varepsilon_\infty = 4.9\ \mathrm{F/m} \pm 20\%$ contributes negligible error. The remaining three quantities, ε_s, τ_r, and σ are parameterized in terms of the sea surface temperature, T_{sea} in °C, and salinity, s in parts per thousand, i.e.,

$$\begin{aligned}
\varepsilon_s(T_{sea}, s) &= \varepsilon_s(T_{sea})\, a_\varepsilon(s, T_{sea}) \\
\varepsilon_s(T_{sea}) &= 87.134 - 1.949\times10^{-1} T_{sea} - 1.276\times10^{-2} T_{sea}^2 + 2.491\times10^{-4} T_{sea}^3 \\
a_\varepsilon(s, T_{sea}) &= 1.0 + 1.613\times10^{-5} s T_{sea} - 3.656\times10^{-3} s + 3.21\times10^{-5} s^2 - 4.232\times10^{-7} s^3
\end{aligned}$$

$$\begin{aligned}
\tau_r(T_{sea}, s) &= \tau_r(T_{sea}, 0)\, b_\varepsilon(s, T_{sea}) \\
\tau_r(T_{sea}, 0) &= 1.768\times10^{-11} - 6.086\times10^{-13} T_{sea} + 1.104\times10^{-14} T_{sea}^2 - 8.111\times10^{-17} T_{sea}^3 \\
b_\varepsilon(s, T_{sea}) &= 1.0 + 2.282\times10^{-5} s T_{sea} - 7.638\times10^{-4} s - 7.76\times10^{-6} s^2 + 1.105\times10^{-8} s^3
\end{aligned} \tag{77}$$

$$\begin{aligned}
\sigma(T_{sea}, s) &= \sigma(25, s)\exp\left(-\Delta B_\varepsilon\right) \\
\Delta &= 25 - T_{sea} \\
B_\varepsilon &= 2.033\times10^{-2} + 1.266\times10^{-4}\Delta + 2.464\times10^{-6}\Delta^2 \\
&\quad - s\left(1.849\times10^{-5} - 2.551\times10^{-7}\Delta + 2.551\times10^{-8}\Delta^2\right) \\
\sigma(25, s) &= s\left(0.182521 - 1.46192\times10^{-3} s + 2.09324\times10^{-5} s^2 - 1.28205\times10^{-7} s^3\right)
\end{aligned}$$

List of Acronyms

ADAPT_MFR	ADAPTive MultiFunction Radar simulator
DFT	Discrete Fourier Transform
GRWAVE	Ground-WAVE propagation program
MLAYER	MultiLAYER tropospheric propagation program
NEMESiS	Naval ElectroMagnetic SImulation System
PRF	Pulse Repetition Frequency
TERPEM	TERrain Parabolic Equation Model

DOCUMENT CONTROL DATA

(Security classification of title, body of abstract and indexing annotation must be entered when the overall document is classified)

1. ORIGINATOR (the name and address of the organization preparing the document. Organizations for whom the document was prepared, e.g. Establishment sponsoring a contractor's report, or tasking agency, are entered in section 8.)

Defence R&D Canada – Ottawa
3701 Carling Avenue, Ottawa, Ontario, K1A 0Z4

2. SECURITY CLASSIFICATION (overall security classification of the document, including special warning terms if applicable)

UNCLASSIFIED

3. TITLE (the complete document title as indicated on the title page. Its classification should be indicated by the appropriate abbreviation (S,C or U) in parentheses after the title.)

A Target Simulation for Studies of Radar Detection in Clutter (U)

4. AUTHORS (Last name, first name, middle initial)

Thomson, A. D.

5. DATE OF PUBLICATION (month and year of publication of document)	6a. NO. OF PAGES (total containing information. Include Annexes, Appendices, etc.)	6b. NO. OF REFS (total cited in document)
October, 2002	60	27

7. DESCRIPTIVE NOTES (the category of the document, e.g. technical report, technical note or memorandum. If appropriate, enter the type of report, e.g. interim, progress, summary, annual or final. Give the inclusive dates when a specific reporting period is covered.)

Technical report

8. SPONSORING ACTIVITY (the name of the department project office or laboratory sponsoring the research and development. Include the address.)

9a. PROJECT OR GRANT NO. (if appropriate, the applicable research and development project or grant number under which the document was written. Please specify whether project or grant)	9b. CONTRACT NO. (if appropriate, the applicable number under which the document was written)
11aa11	

10a. ORIGINATOR'S DOCUMENT NUMBER (the official document number by which the document is identified by the originating activity. This number must be unique to this document.)	10b. OTHER DOCUMENT NOS. (Any other numbers which may be assigned this document either by the originator or by the sponsor)
DRDC Ottawa TR 2002-145	

11. DOCUMENT AVAILABILITY (any limitations on further dissemination of the document, other than those imposed by security classification)

(X) Unlimited distribution
( ) Distribution limited to defence departments and defence contractors; further distribution only as approved
( ) Distribution limited to defence departments and Canadian defence contractors; further distribution only as approved
( ) Distribution limited to government departments and agencies; further distribution only as approved
( ) Distribution limited to defence departments; further distribution only as approved
( ) Other (please specify):

12. DOCUMENT ANNOUNCEMENT (any limitation to the bibliographic announcement of this document. This will normally correspond to the Document Availability (11). However, where further distribution (beyond the audience specified in 11) is possible, a wider announcement audience may be selected.)

13. ABSTRACT (a brief and factual summary of the document. It may also appear elsewhere in the body of the document itself. It is highly desirable that the abstract of classified documents be unclassified. Each paragraph of the abstract shall begin with an indication of the security classification of the information in the paragraph (unless the document itself is unclassified) represented as (S), (C), or (U). It is not necessary to include here abstracts in both official languages unless the text is bilingual).

A high fidelity simulation of the coherent signal samples produced by a low-PRF shipborne pulsed Doppler radar when observing a sea-skimming anti-ship missile moving through precipitation above the sea has been created. The modelled radar system uses a phased array antenna and has the ability to vary the parameters of the transmitted waveform from burst to burst. The output of the simulation is designed for combination with the output of clutter and signal processor simulations so that target detection in clutter can be examined. A complete description of the physical models used in the simulation and their mathematical implementation is presented. Example output data were used to derive propagation factor values, which were then compared with the output of the TERPEM commercial software package. Received power values were also derived from the example data and compared with the output of a multifunction radar simulator (ADAPT_MFR). Good agreement between the data sets was achieved, except for expected differences found at ranges near the radar horizon ("intermediate region"). Thus, this simulation is capable of producing realistic and useful signals for target detection studies. It is recommended that the simulation be upgraded by integrating the TERPEM software. This will allow propagation to be correctly considered near and beyond the radar horizon, thus extending the applicability of the simulation.

14. KEYWORDS, DESCRIPTORS or IDENTIFIERS (technically meaningful terms or short phrases that characterize a document and could be helpful in cataloguing the document. They should be selected so that no security classification is required. Identifiers such as equipment model designation, trade name, military project code name, geographic location may also be included. If possible keywords should be selected from a published thesaurus. e.g. Thesaurus of Engineering and Scientific Terms (TEST) and that thesaurus-identified. If it is not possible to select indexing terms which are Unclassified, the classification of each should be indicated as with the title.)

radar, target, missile, clutter, precipitation, phased array, propagation

Defence R&D Canada

Canada's leader in defence
and national security R&D

R & D pour la défense Canada

Chef de file au Canada en R & D
pour la défense et la sécurité nationale

www.drdc-rddc.gc.ca